# Fault-valve behavior estimated from intensive foreshocks and aftershocks of the 2017 M 5.3 Kagoshima Bay earthquake sequence, Kyushu, southern Japan

**Yoshiaki Matsumoto[1 †], Keisuke Yoshida[1*], Toru Matsuzawa[1], and Akira Hasegawa[1]**

[1] Research Center for Prediction of Earthquakes and Volcanic Eruptions, Graduate School of Science, Tohoku University, Sendai 980, Japan

[†] Now at Japan Meteorological Agency, Japan

*Corresponding author: Keisuke Yoshida (keisuke.yoshida.d7@tohoku.ac.jp)

**Key Points:**

- Intensive foreshocks migrate via one plane.
- Aftershock hypocenters migrate toward shallower levels via several planes.
- Upward pore pressure migration explains the occurrence of the foreshock–mainshock–aftershock sequence.

## Abstract

Determining fluid migration and pore pressure changes within the Earth is key to understanding earthquake occurrences. We investigated the spatiotemporal characteristics of intense fore- and aftershocks of the 2017 $M_L$ 5.3 earthquake in Kagoshima Bay, Kyushu, southern Japan, to examine the physical processes governing this earthquake sequence. The results show that the foreshock hypocenters moved upward on a sharply defined plane with steep dip. The mainshock hypocenter was located at the edge of a seismic gap formed by foreshocks along the plane. This spatial relationship suggests that the mainshock ruptured this seismic gap. The corner frequency of the mainshock supports this hypothesis. The aftershock hypocenters migrated upward along several steeply dipped planes. The aftershock activity slightly differs from the simple mainshock–aftershock type, suggesting that aseismic processes controlled this earthquake sequence. We established the following hypothesis: First, fluids originating from the subducting slab migrated upward and intruded into the fault plane, reducing the fault strength and causing a foreshock sequence and potentially aseismic slip. The continuous decrease in the fault strength associated with an increase in the pore pressure and the increase in shear stress associated with aseismic slip and foreshocks caused the mainshock in an area with relatively high fault strength. The change in the pore pressure associated with post-failure fluid discharge contributed to aftershocks, causing the upward migration of the earthquake. These observations demonstrate the importance of considering fluid movement at depth not only earthquake swarms but also foreshock-–mainshock–aftershock sequences.

## 1 Introduction

An earthquake is a natural phenomenon during which a high-speed rupture propagates along a fault. Two factors control the occurrence of an earthquake: an increase in the shear stress acting on the fault and a decrease in the fault strength. The results of previous studies suggested that the increase in the pore pressure plays an important role in the earthquake occurrence (e.g., Hasegawa, 2017; Hubbert & Rubey, 1959; Nur & Booker, 1972; Sibson, 1992; Rice, 1992) because it reduces the fault strength.

A well-known example of fluid-driven seismicity is the seismicity induced by fluid injection for engineering purposes (e.g., Ellsworth, 2013). There is also growing evidence that natural earthquake swarms are closely related to fluid movement at depth. In fact, the characteristics of many natural seismic swarms are similar to those of fluid injection-induced seismicity including the migration behavior of the earthquake hypocenter (e.g., Fischer and Horálek, 2003; Parotidis et al., 2003; Bianco et al., 2004; Yukutake et al., 2011; Shelly et al., 2016; Yoshida et al., 2016a; Ruhl et al., 2016; De Barros et al., 2019). Based on the determination of the hypocenters and focal mechanisms of earthquake swarm at the 2009 Hakone volcano, the diffusion of high-pressure fluid triggered the swarm (Yukutake et al., 2011). The spatiotemporal evolution of seismic activity in the Long Valley Caldera, California, indicates that a pore pressure transient with a low-viscosity fluid initiated and sustained the swarm in 2014 (Shelly et al., 2016). It has been hypothesized that several earthquake swarms that occurred after the 2011 Tohoku-Oki earthquake were triggered by a decrease in the fault strength due to upward pore pressure migration (Terakawa et al., 2013; Okada et al., 2016; Yoshida et al., 2016a, 2019a).

Not only earthquake swarms but also foreshock–mainshock–aftershock sequences may be closely related to the fluid behavior in the Earth interior. Sibson (1992) established the fault-

63 valve model in which the pore pressure cycle controls the earthquake cycle due to
64 overpressurized fluids that rise from the deeper portion of the fault. In this model, fault ruptures
65 create a transient fracture permeability within the fault zone, which acts as a valve, promoting
66 the upward discharge of fluids from deeper portions of the crust. This model is supported by
67 various geological and geophysical observations (Sibson, 2020). Hasegawa et al. (2005)
68 proposed a model for the deformation process in a subduction zone based on various geophysical
69 observations including seismic tomography data obtained for northeastern Japan. In this model,
70 fluids expelled from the subducting slab migrate upward, reach the crust, and cause anelastic
71 crustal deformation including earthquakes.

72 The migration characteristics of earthquake hypocenters can be used to infer the origin of
73 the seismicity (e.g., Yukutake et al., 2011; Ruhl et al., 2016; Yoshida & Hasegawa, 2018a,b; De
74 Barros et al., 2019). Pore pressure migration and aseismic slip propagation are typical
75 mechanisms attributed to the migration of earthquakes. In the former mechanism, the hypocenter
76 migration is presumed to reflect the migration of fluids (e.g., Shapiro et al., 1997; Talwani et al.,
77 2007). In the latter mechanism, the hypocenter migration is presumed to be a result of aseismic
78 slip propagation (e.g., Lohman & McGuire, 2007; Roland & McGuire, 2009). The
79 spatiotemporal distribution of earthquake hypocenters can be more precisely estimated than other
80 seismological characteristics such as the three-dimensional seismic velocity structure. By
81 examining relocated hypocenters, we may extract information on aseismic physical processes
82 controlling earthquakes, which is crucial to understanding the earthquake generation. The results
83 of previous studies showed that the seismic activity caused by aseismic processes differs from
84 that of the mainshock–aftershock sequence (e.g., Hainzl & Ogata, 2005; Roland & McGuire,
85 2009; Kumazawa & Ogata, 2013; Yoshida & Hasegawa, 2018b). This suggests that

investigations of the seismicity may provide clues about aseismic processes governing earthquakes.

The volcanic front on Kyushu Island in southern Japan formed due to the subduction of the Philippine Sea Plate. Several of the most active volcanoes in Japan are distributed along this volcanic front (e.g., Sakurajima and Aso). Kagoshima Bay is located at this volcanic front (Fig. S1), which is characterized by a low-gravity anomaly that extends from north to south. On July 11, 2017, an $M_L$ 5.3 strike-slip earthquake occurred at a depth of ~10 km in Kagoshima Bay (Fig. 1). Seismicity activity had been recorded near the mainshock hypocenter since December 2016 (Fig. 1c). In total, 1.843 foreshock events were recorded and listed in the Japan Meteorological Agency (JMA) unified seismic catalogue. The seismicity increased after the mainshock; 12.595 events are listed in the JMA catalogue. Based on the focal mechanisms of earthquakes in this region, these events were of strike-slip type with a NW–SE P-axis (Fig. 1b). Only a small coseismic step was detected by the national GNSS (Global Navigation Satellite System) network (Fig. S2). Based on the spatiotemporal variation in the b-value and the migration of the hypocenters, Nanjo et al. (2018) suggested that fluid movement caused the earthquake sequence in Kagoshima Bay, but the detailed physical process controlling this foreshock–mainshock–aftershock sequence remains unclear.

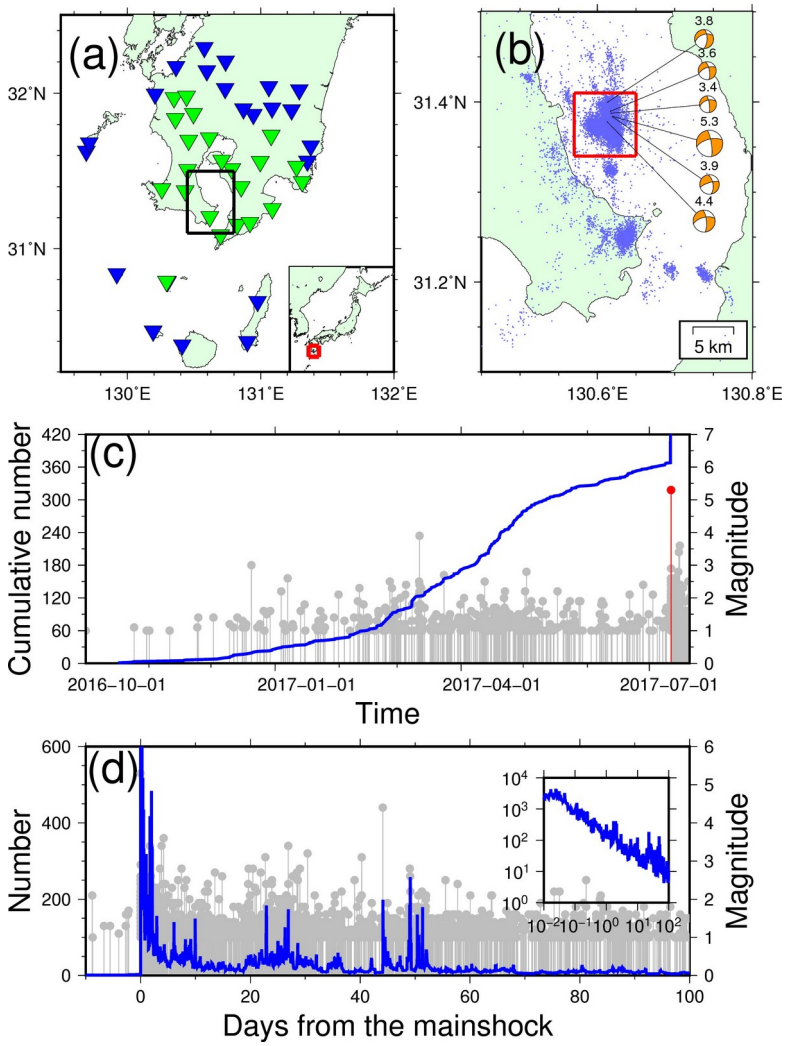


**Figure 1**. (**a**) Map showing southern Kyushu. Inverted triangles indicate the seismic stations. We used arrival time data obtained at both blue and green stations. We analyzed waveform data recorded at the green stations. The black square shows the study area. (**b**) Hypocenter distribution of earthquakes that occurred in Kagoshima Bay from January 1, 2003, to April 8, 2018, and their focal mechanisms. The hypocenters and focal mechanisms were extracted from the JMA unified catalog. The red square is defined as "the area surrounding the mainshock hypocenter" in this study. The numbers above the focal mechanisms indicate the JMA magnitude of each earthquake. (**c**) M–T diagram and cumulative number of $M_{JMA} \geq 1.0$ earthquakes that occurred in the area surrounding the mainshock hypocenter (i.e., red square in Fig. 1b) prior to

the mainshock. The vertical red line denotes the mainshock. (**d**) Aftershock occurrence rate of events with a magnitude $M_{JMA} \geq 1.0$ (blue) and corresponding M–T diagram (gray). The inset shows the correlation between the aftershock occurrence rate and time on a log-log scale. The occurrence rate was estimated by calculating the reciprocal of the time during which 10 events with $M_{JMA} \geq 1.0$ occurred.

In this study, we examined the physical processes that controlled the $M_L$ 5.3 Kagoshima Bay earthquake sequence in Kyushu, southern Japan. First, we determined the hypocenters and focal mechanisms of this earthquake sequence and delineated the fault structure. We also estimated the size of the mainshock and examined its relationship with the fore- and aftershocks to obtain a comprehensive view of this foreshock–mainshock–aftershock sequence. We then examined the spatiotemporal characteristics of the intense fore- and aftershocks to extract information about the aseismic phenomena governing this earthquake sequence. Finally, by integrating the observations, we established a model that can be used to explain the occurrence and characteristics of the foreshock–mainshock–aftershock sequence associated with the 2017 M5.3 Kagoshima Bay earthquake.

## 2 Methods

### 2.1 Hypocenter relocations

We relocated 21.102 events listed in the JMA unified catalogue for the southern Kagoshima Bay region for the period from March 1, 2003 to April 8, 2018 using the Double-Difference (DD) method (Waldhauser & Ellsworth, 2000). This relative relocation method minimizes the residuals between the observed and theoretical travel time differences for adjacent earthquake pairs at each station. We applied the DD method to differential arrival time data, which were estimated from the waveform cross-correlation, and those listed in the JMA unified catalog. The procedure was identical to that reported in Yoshida and Hasegawa (2018a, b), which can be briefly described as follows.

First, we obtained precise differential arrival time data using waveform cross-correlations. We used the waveform data observed at 20 permanent seismic stations surrounding the focal area (Fig. 1a; green stations). At each station, the ground velocity was measured using three-component short-period seismometers (natural period of 1s) and a sampling rate of 100 Hz. We applied a 5–12 Hz Butterworth filter to the waveforms of each target event. We used 2.8 and 4.3 s time windows for the P- and S-waves, respectively, starting 0.3 s before their arrival. The arrival times were obtained from the JMA unified catalogue. If arrival times were not available, they were estimated using the one-dimensional JMA2001velocity model (Ueno et al., 2002) and the hypocenters, and origin times listed in the JMA unified catalogue. We calculated the waveform cross-correlations of event pairs with hypocenters within 3 km from each other and obtained differential arrival times when the cross-correlation coefficients were greater than 0.8. In total, we acquired 17.332.318 P-wave differential arrival time data points and 27.738.043 S-wave data points. We also derived the differential arrival data from the arrival time data listed in

the JMA unified catalog: 474.670 data for P-waves and 543.226 data for S-waves. For the mainshock, only data derived from the JMA unified catalog were used because of its long duration.

Second, we applied the hypo-DD algorithm (Waldhauser & Ellsworth, 2000) to the differential arrival time data. We used a spherical shell two-layer model (Aki, 1965) for the hypocenter relocation. In this model, the seismic velocities in each layer are proportional to the power of the distance from the center of the Earth (Figure S3). The medium parameters were determined for consistency with the seismic tomography results obtained in the Kyushu region (Saiga et al., 2010). We used the hypocenters listed in the JMA unified catalogue for the initial locations for the relocation. Figures 2a and 3a show the distribution of these initial hypocenters. Differential arrival time data were weighted with respect to the square root of the cross-correlation coefficient. The hypocenters were updated after 50 iterations of the relocation procedure. During the first ten iterations, a higher weight was assigned to the catalogue data to constrain the relative locations of large-scale features. In the latter 40 iterations, a higher weight was assigned to the data derived by the cross-correlations to delineate shorter-scale features. We evaluated the uncertainty in the relative hypocenter locations by recalculating the hypocenters 200 times based on bootstrap resampling of differential arrival time data.

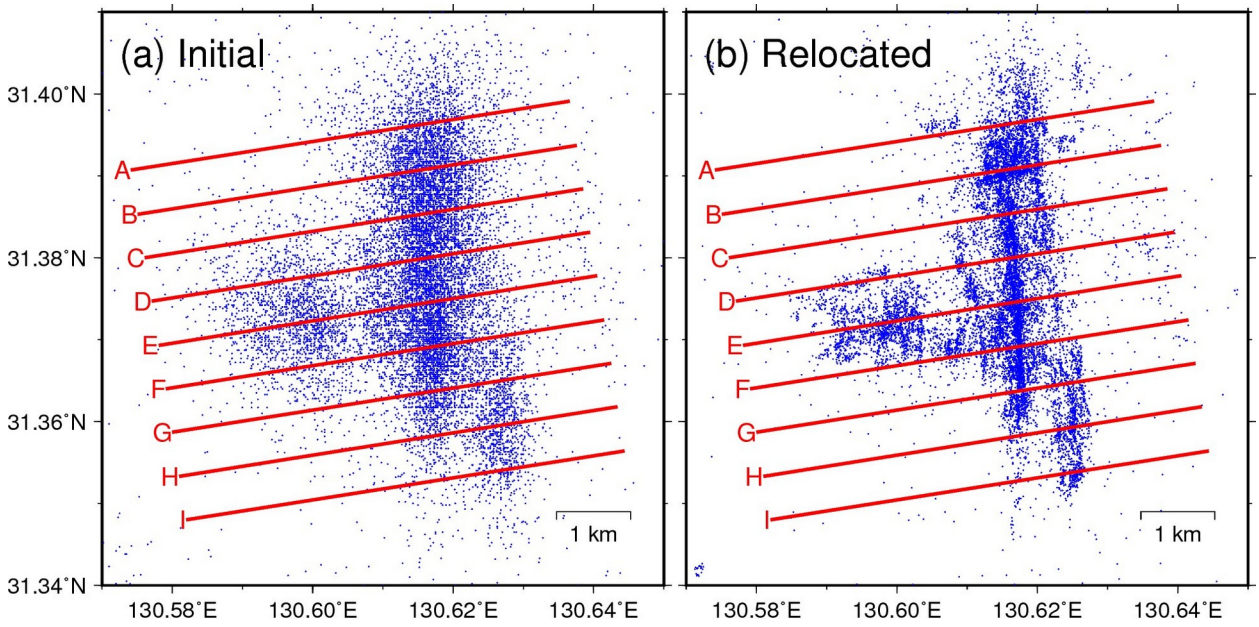


**Figure 2.** Maps showing the distribution of the (**a**) initial hypocenters listed in the JMA unified catalog and (**b**) relocated hypocenters based on the DD method. Blue dots indicate the locations of the hypocenters. The red lines labeled A to I indicate the locations of the vertical sections shown in Figure 3.

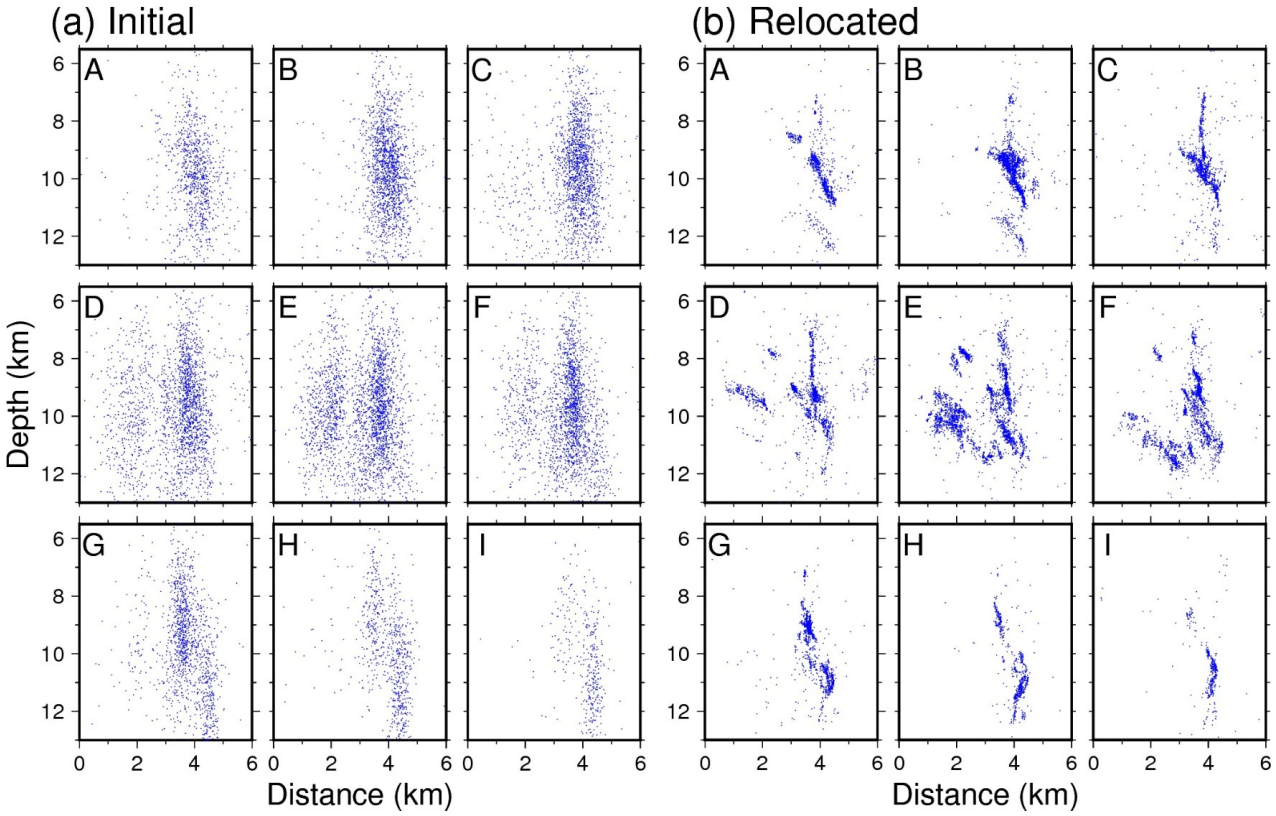


**Figure 3.** Cross-sectional views showing the distribution of the (**a**) initial hypocenters listed in the JMA unified catalog and (**b**) relocated hypocenters based on the DD method. Blue dots indicate the locations of the hypocenters. The nine figures (A–I) represent the cross-sectional views along the vertical sections indicated by the red lines in Fig. 2.

## 2.2 Estimation of focal mechanisms

We estimated the focal mechanisms based on the amplitude ratios of the waveforms using the method of Yoshida et al. (2019b), which is similar to that of Dahm (1996). We used six focal mechanisms determined by the JMA (Fig. 1b) to represent effects of the path and site on the waveform. We determined the focal mechanisms of 161 earthquakes with $M_L \geq 2$. We used displacement waveforms obtained by integrating the velocity waveforms recorded at the 20 stations (green triangles in Fig. 1a) surrounding the hypocenters. The vertical component was used for the analysis of the P-wave, whereas radial and transverse components were used for that of the S-wave. We applied a 2–5 Hz bandpass filter to the waveforms, cutting them out with time windows of 2.8 s for P-waves and 4.3 s for S-waves starting 0.3 s before their arrival.

We used waveform cross-correlations to measure the amplitude ratios between target and reference events. The amplitude ratios were obtained for pairs with absolute correlation coefficients above 0.75. We used principal component analysis (PCA) to measure the amplitude ratios.

We only estimated the mechanism solutions when amplitude ratios were obtained for more than 20 channels. We eliminated the results when the Variance Reduction (VR) was below 80:

$$VR = \left( 1 - \frac{\sum_{k=1}^{n} \left( d_k - s_k \right)^2}{\sum_{k=1}^{n} d_k^2} \right) \cdot 100, \quad (1)$$

where $d_k$ and $s_k$ are the observed and calculated displacement amplitude ratios, respectively, at channel $k$.

### 2.3 Estimation of the size of the mainshock source

We estimated the size of the mainshock source based on the circular crack source model (e.g., Sato & Hirasawa, 1973; Madariaga, 1976). In this source model, the source radius is related to the S-wave corner frequency, $f_c$, as follows:

$$r = \frac{k\beta}{f_c}, \tag{2}$$

where $r$ is the source radius, $k$ is a constant, and $\beta$ is the S-wave velocity close to the source. Based on a rupture velocity of $0.9\beta$, $k$ is 0.44 in the model of Sato and Hirasawa (1973) and 0.32 in the model of Madariaga (1976) for P-waves (Kaneko & Shearer, 2014). Because the estimated source size depends on the source model, we computed the fault size using both models. We assumed a $\beta$ value of 3.4 km/s.

We used the spectral ratio method (e.g., Imanishi & Ellsworth, 2006) to estimate the corner frequency of the mainshock. In this method, effects of the propagation and location on the seismic wave are empirically removed using the waveforms of an adjacent small earthquake (empirical Green's function, EGF, event). Based on the assumption that the source spectrum, that is, $S_j(f)$, follows the $\omega^2$ model (Aki, 1967; Brune, 1970), the theoretical ratio between the velocity spectra of the mainshock, $v_i(f)$, and the EGF event, $v_i^{egf}(f)$, at station $i$ can be calculated as follows:

$$SSR_{ij}(f) = \frac{v_i(f)}{v_i^{egf}(f)} = \frac{M_0}{M_0^{egf}} \frac{R_{\theta\varphi i}}{R_{\theta\varphi i}^{egf}} \frac{1+\left(\frac{f}{f_c^{egf}}\right)^2}{1+\left(\frac{f}{f_c}\right)^2}, \tag{3}$$

where $M_0$ and $M_0^{egf}$ are the seismic moments of the target earthquake and EGF event, respectively; $R_{\theta\varphi ij}$ and $R_{\theta\varphi i}^{egf}$ are their radiation patterns at station$i$, respectively; and $f_c^{egf}$ is the

229 corner frequency of the EGF event. Based on Eq. (3), $f_c$ can be estimated from the spectral
230 ratios.

231 We calculated the spectral ratios by using P-wave velocity waveforms observed at the 20
232 stations surrounding the source area (green inverted triangles in Fig. 1b). The EGF events were
233 earthquakes with M ≥ 2 and a distance from the mainshock below 1.0 km based on the relocated
234 hypocenters. The following procedure was performed (Yoshida et al., 2017):

235 (1) For the target mainshock and EGF events, the waveforms of the three components were
236 extracted from a 2.0 s time window starting 0.3 s before the arrival of the P-wave at each
237 station. The multitaper method (Thomson, 1982; Prieto et al., 2009) was applied to
238 calculate the spectra.

239

240 (2) For channels with EGF observation spectra with a signal-to-noise ratio > 4 at all
241 frequencies from 0.5 to 30.0 Hz, the spectral ratio between the mainshock and EGF event
242 was calculated. We used waveforms up to 0.3 s before the arrival of the P-waves for the
243 noise window.

244

245 (3) We calculated the geometric mean of the spectral ratios $GSR(f)$ of all channels at each
246 frequency for the EGF events, which satisfied the above-mentioned criterion at five or
247 more stations:

248 $$GSR(f)=\prod_{i=1}^{N}\left(SR_i(f)\right)^{\frac{1}{N}}, \quad (4)$$

249 where $SR_i(f)$ is the observed spectral ratio obtained at station*i* and $N$ is the number of
250 stations.

251

252 (4) By using the grid search and minimizing the evaluation function $J$, the corner
253 frequencies of the mainshock, $f_c$, and EGF event, $f_c^{egf}$, were determined:

$$J=\sum_{k=1}^{n_{freq}}\left|\log\left(GSR\left(f_k\right)\right)-A\log\left(NSR\left(f_k;f_c,f_c^{egf}\right)\right)\right|, \quad (5)$$

255 where $NSR\left(f;f_c,f_c^{egf}\right)=\frac{1+\left(f/f_c^{egf}\right)^2}{1+\left(f/f_c\right)^2}$, $n_{freq}$ is the number of frequencies, and $f_k$ is frequency
256 (at 0.5 Hz intervals from 0.5 to 30 Hz). The grid search was performed for $f_c$ and $f_c^{egf}$ by
257 assuming a range from 0.1 to 100 Hz at 0.1 Hz steps. The amplitude ratio, $A$, was
258 estimated using the least squares method for each grid search step.
259

260 We applied the spectral ratio method to 33 EGF candidates. We obtained spectral ratios for
261 13 EGF events, which satisfy our S/N ratio and data criteria. Figure S4 shows the spectral ratios
262 of the 13 EGF events.
263

264 **2.4 Detection of aseismic processes from seismicity**

265 The Epidemic Type Aftershock Sequence (ETAS) model (Ogata, 1988), which is based on the
266 superposition of the modified Omori law (Ustu, 1961), can be used to explain mainshock–
267 aftershock seismicity. The ETAS model assumes that the seismicity rate is the sum of the
268 background rate of independent events, $\lambda_0$, and aftershocks triggered by each event, $\lambda_i(t)$:

$$\lambda(t)=\lambda_0+\sum_{i:t_i<t}\lambda_i(t). \quad (6)$$

270 Based on the modified Omori law, each earthquake can trigger its own aftershock sequence
271 (Utsu et al., 1995):

$$\Lambda_i(t) = \frac{K_0}{(c + t - t_i)^p} e^{\alpha(M_i - M_{min})}, \quad (7)$$

where $t_i$ is the occurrence time; $M_i$ is the magnitude of each event, $i$, that occurred prior to time $t$ ; $M_{min}$ is the magnitude of completeness of the earthquake catalogue; $K_0$, $c$, and $p$ are constants; and $t$ is the time that has elapsed since the main event.

We applied the ETAS model to the seismicity observed after the mainshock in Kagoshima Bay and investigated the difference between the simulated and observed seismicity. The results show that the foreshock activity cannot be explained by the ETAS model, likely because aseismic processes mainly controlled the foreshock activity. We used the timings and magnitudes of the earthquakes listed in the JMA catalogue. The lower limit of the magnitude, $M_C$, was set to 1.0. Figure S4 shows the magnitude–frequency distribution. The distribution follows the Gutenberg–Richter law (Gutenberg & Richter, 1944) when $M_{JMA} \geq 1.0$. The SASeis2006 algorithm by Ogata (2006) was used to estimate the model parameters and calculate the residuals of the ETAS model.

## 3 Results

### 3.1 Fault structure and seismic gap

We obtained the relocated hypocenters of 20.347 events and the focal mechanisms of 61 events. Almost all events in the Kagoshima Bay earthquake sequence can be accurately relocated with the DD algorithm. The location data for 755 earthquakes were removed because their hypocenters were located above the ground surface or they contained outliers in the differential arrival time data. We computed the differences between the maximum and minimum values in the 95% confidence interval of the hypocenter locations (Fig. S6) estimated from the bootstrap

294 resampling and obtained the medians as a measure of the estimation error of the relative location:
295 0.0013 ° in longitude, 0.0011° in latitude, and 0.42 km in depth.
296 Figures 2b and 3b show the distribution of the relocated hypocenters. Movie 1 shows the
297 animation of the cross-sectional views of the hypocenters along various lines. Most hypocenters
298 are located within ~5 km from the mainshock hypocenter and are distributed along several
299 planes. These characteristics are in contrast to the distribution of the initial hypocenters (Figs 2a
300 and 3a), which were scattered three-dimensionally, similar to a cloud. This significant change in
301 the hypocenter distribution is due to the improvements of the relative locations of the
302 hypocenters in this study based on the use of many accurate differential arrival time data. Similar
303 improvements of the relative hypocenters, from cloud-like distribution to planar structures, were
304 previously reported for shallow earthquakes in Japan based on a similar method and data (e.g.,
305 Yoshida & Hasegawa, 2018a, b). The cloud-like distribution of the initial hypocenters reflects the
306 errors in the hypocenter locations in the JMA unified catalog, which are due to errors in the
307 manual selection.
308 Figure 4 shows the spatial distribution of the focal mechanisms. Because the reference
309 focal mechanisms are in the northern part of the source region (Fig. 1b), newly estimated focal
310 mechanisms are mainly located in the northern part. The figure shows that the nodal planes of
311 most focal mechanisms are parallel to the planar structures of the hypocenters, suggesting that
312 individual small earthquakes occurred on several macroscopic planes.
313

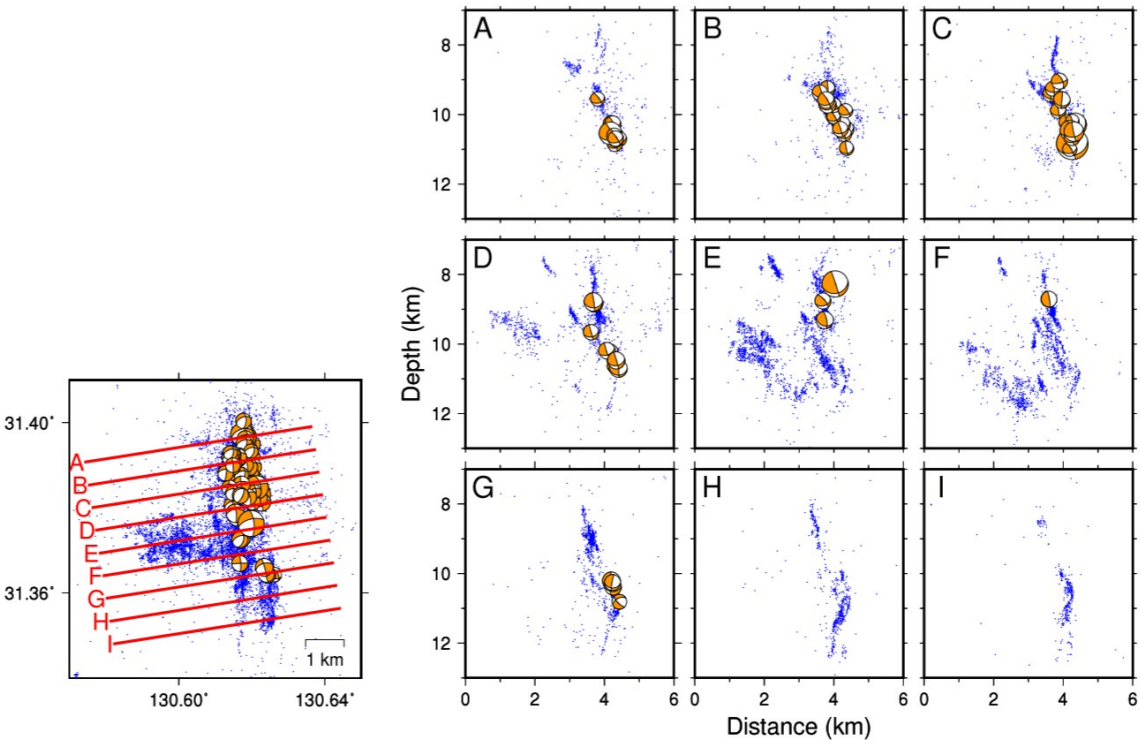


314
315

316 **Figure 4.** Estimated focal mechanisms plotted on the hypocenter distribution. The left figure is a
317 map view and the nine figures (A–I) on the right are cross-sectional views along vertical sections
318 indicated by the red lines in the left figure.

319

320 Based on Figs 2b, 3b and 4, the fault structures of the 2017 Kagoshima Bay earthquake
321 sequence are complex, consisting of several subparallel planes. However, the distribution of the
322 hypocenters was relatively simple before the mainshock. Figure 5 shows an enlarged view of the
323 spatial distribution of the hypocenters of the foreshocks (red dots). Most hypocenters are evenly
324 distributed in one plane, with a strike parallel to those of the nodal planes of the focal
325 mechanisms of the mainshock and individual small earthquakes, suggesting that the mainshock
326 and most of the foreshocks occurred on this plane.

327

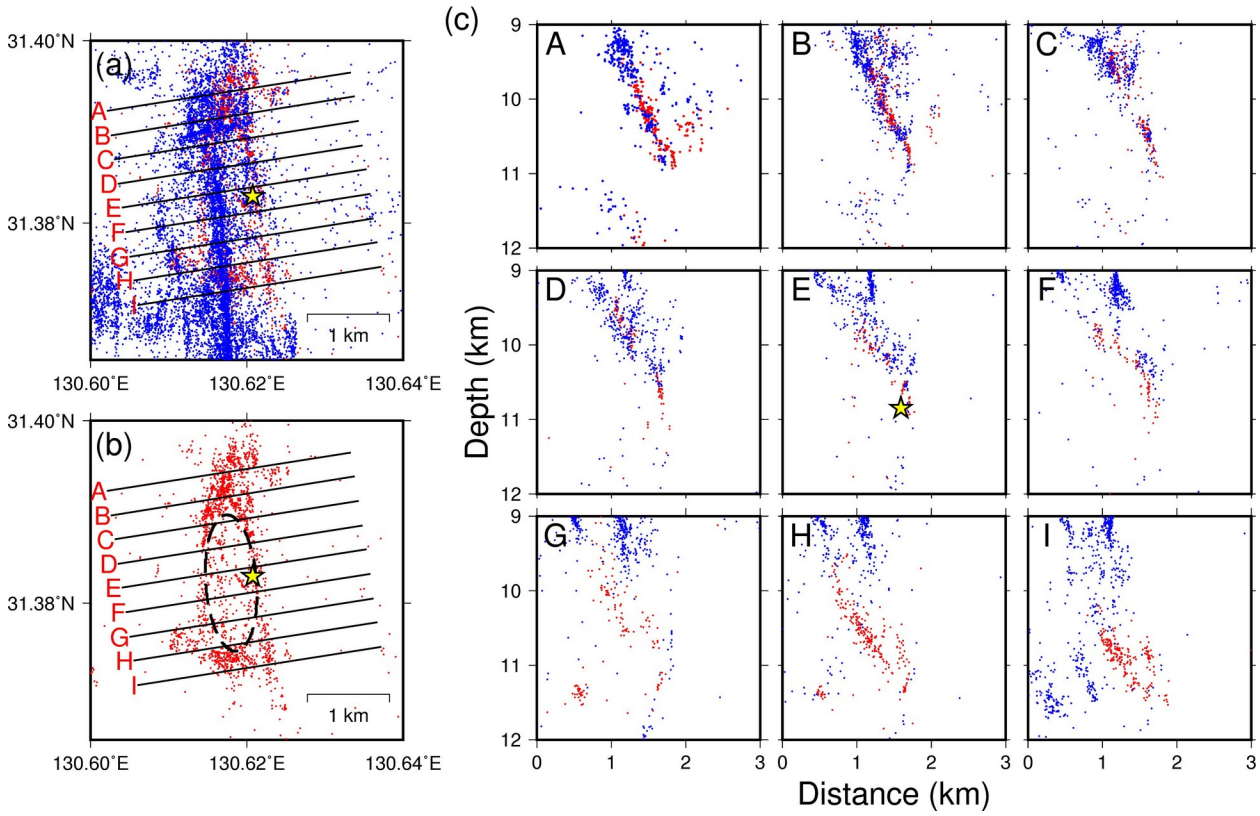


**Figure 5.** Hypocenter distribution of the foreshocks. Red and blue circles represent the hypocenters of foreshocks and aftershocks, respectively, Blue circles represent the hypocenters of the precursory activity. (**a**) Map showing the hypocenters of the precursor activity and aftershocks. (**b**) Map showing only the hypocenters of the precursory activity. The broken ellipse indicates the location of the seismic gap. (**c**) Cross-sectional views along vertical sections A to I shown in (**a**). The yellow star indicates the hypocenter location of the mainshock.

The hypocenters of the foreshocks are not uniformly distributed in the plane, but they are distributed in form of a doughnut, that is, a seismic gap forms in the center of the plane (broken ellipse in Fig. 5b). To demonstrate this distribution, we estimated the lateral distribution of the

341 moment release on the fault (Fig. 6a) during the foreshock sequence following Yoshida et al.
342 (2020a). We computed the seismic moment release of each earthquake by assuming that its
343 magnitude is equal to the moment magnitude. Subsequently, we summed the moment release
344 values of the points that were evenly spaced every 0.04 km by using the earthquakes within the
345 nearest grid cell. The result shown in Fig. 6b indicates that the moment release of the foreshock
346 sequence is smaller (¿ $10^{11}\,Nm$) in the region corresponding to the seismic gap than in the
347 surrounding region (¿ $10^{11}\,Nm$). The hypocenter of the mainshock is located at the edge of this
348 seismic gap. Figure 5 shows a comparison of the hypocenters of the foreshocks and aftershocks.
349 Although aftershocks occur inside the seismic gap based on the map (Fig. 5a), they actually
350 occur in shallower areas than the foreshocks (Fig. 5c), that is, not within the seismic gap of the
351 foreshocks.
352

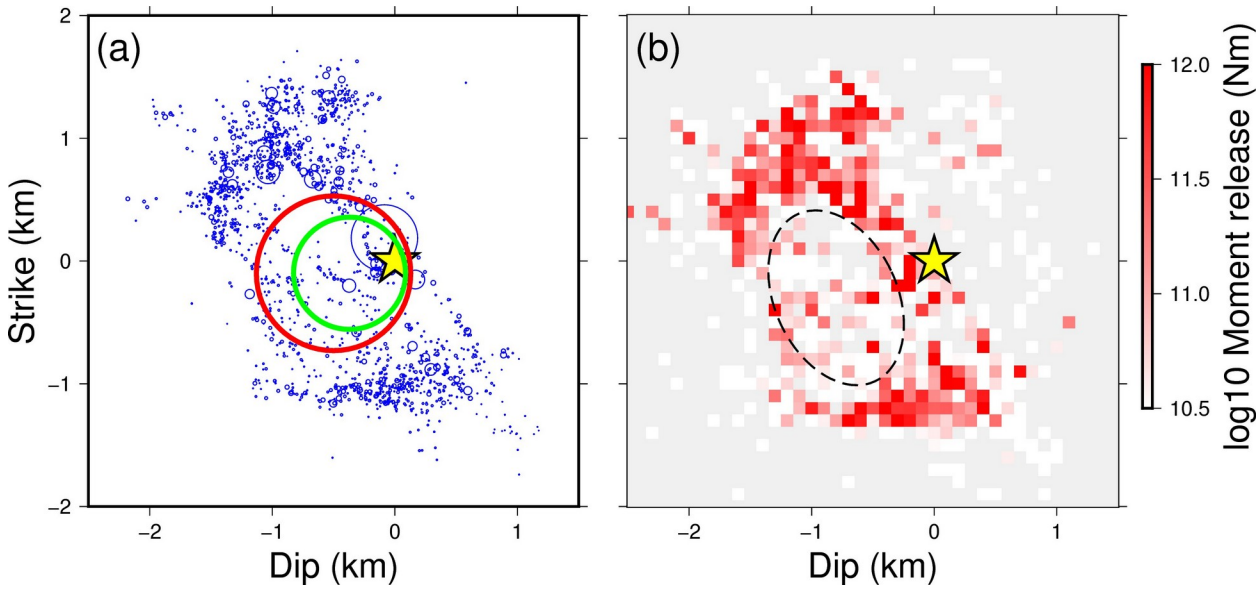


353
354

355 **Figure 6.** Seismic gap of earthquakes in the foreshock period projected on the dominant plane.
356 (**a**) Comparison of the size of the seismic gap with the estimated sizes of the faults associated

with the mainshock. Blue circles indicate the hypocenters of the precursory activity corresponding to the fault sizes by assuming stress drops of 10 MPa. The yellow star indicates the location of the mainshock hypocenter. The red circle represents the size of the fault corresponding to the mainshock estimated based on the model of Sato and Hirasawa (1973). The green circle represents the size of the fault corresponding to the mainshock estimated based on the model of Madariaga (1976). (**b**) Moment release amount (color scale) computed for each 0.04 km grid cell. The broken ellipse represents the seismic gap.

The median value of the estimated corner frequencies of the mainshock is 1.9 Hz (Fig. S4). The first and third quartiles are 1.8 and 2.5 Hz, respectively. Based on the median corner frequency and the models proposed by Sato and Hirasawa (1973) and Madariaga (1976), the source radius of the mainshock is 787 and 572 m, respectively. It is much smaller than the foreshock and aftershock regions but comparable to the seismic gap (Fig. 6a).

### 3.2 Foreshock and aftershock migration

Figures 7a–c show the occurrences of the foreshocks on a color scale. In Figs 8a–c, the occurrence of each earthquake is compared with the longitude, latitude, and depth, respectively, to illustrate their migration behavior. In the longitudinal direction (Fig. 8a), the hypocenters expand nearly symmetrically in the first 230 days of foreshock activity and concentrate in the east close to the hypocenter of the mainshock during the last ~70 days. In the latitudinal direction (Fig. 8b), the hypocenters migrate from north to south. In the depth direction (Fig. 8c), the hypocenters migrate both in the shallow and deep directions, indicating that most earthquakes

380 occurred in the deeper part surrounding the mainshock hypocenter during the last ~70 days of
381 activity.

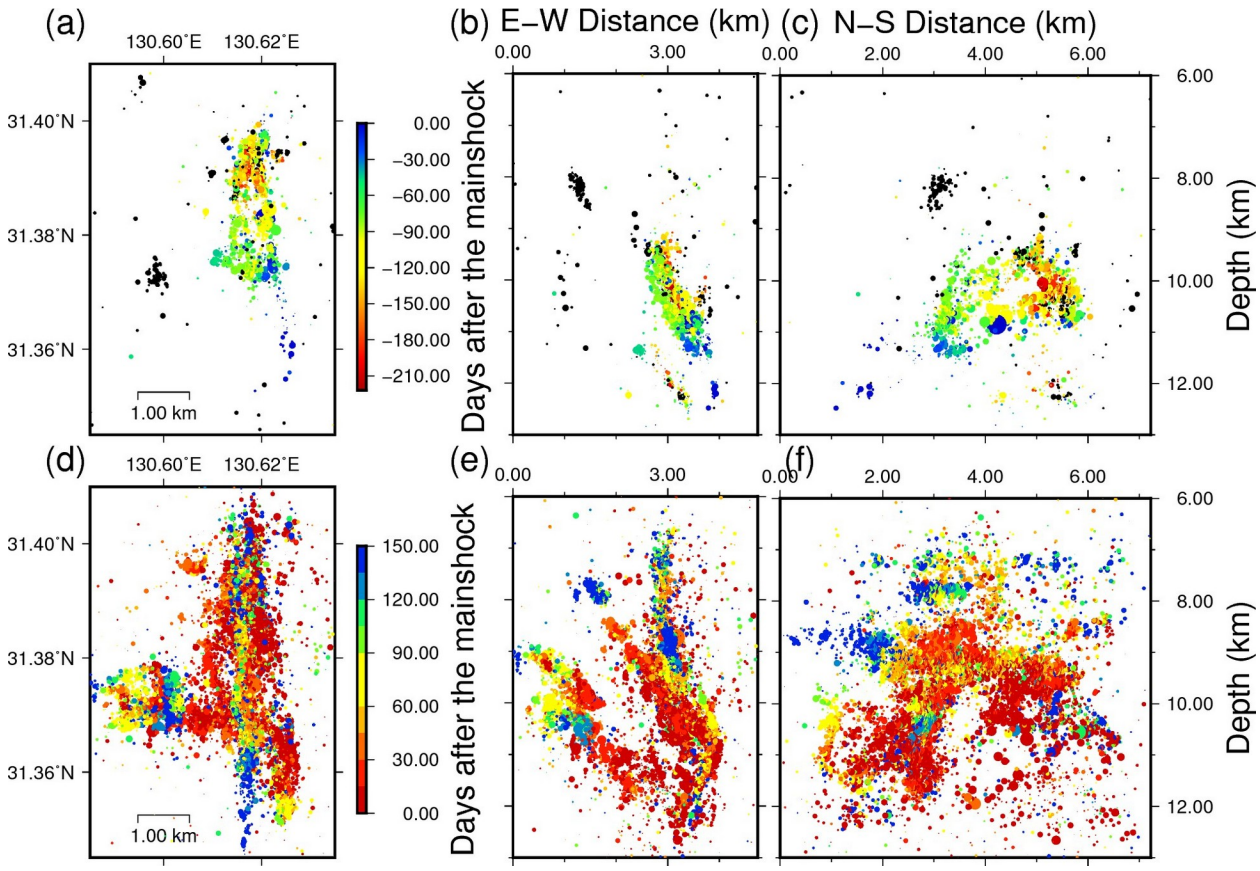

382
383

384 **Figure 7.** Spatiotemporal evolution of the hypocenters (**a**)–(**c**) before and (**d**)–(**f**) after the
385 mainshock. (**a**) Projection of the hypocenters, (**d**) map view, (**b**) and (**e**) east–west cross section,
386 and (**c**) and (**f**) north–south cross section. The symbol sizes corresponds to the JMA magnitude.
387 The hypocenters are colored according to their occurrence time measured relative to that of the
388 mainshock, that is, the mainshock occurred at time 0 and negative and positive numbers denote
389 the days before and after the mainshock, respectively.
390
391

392

393

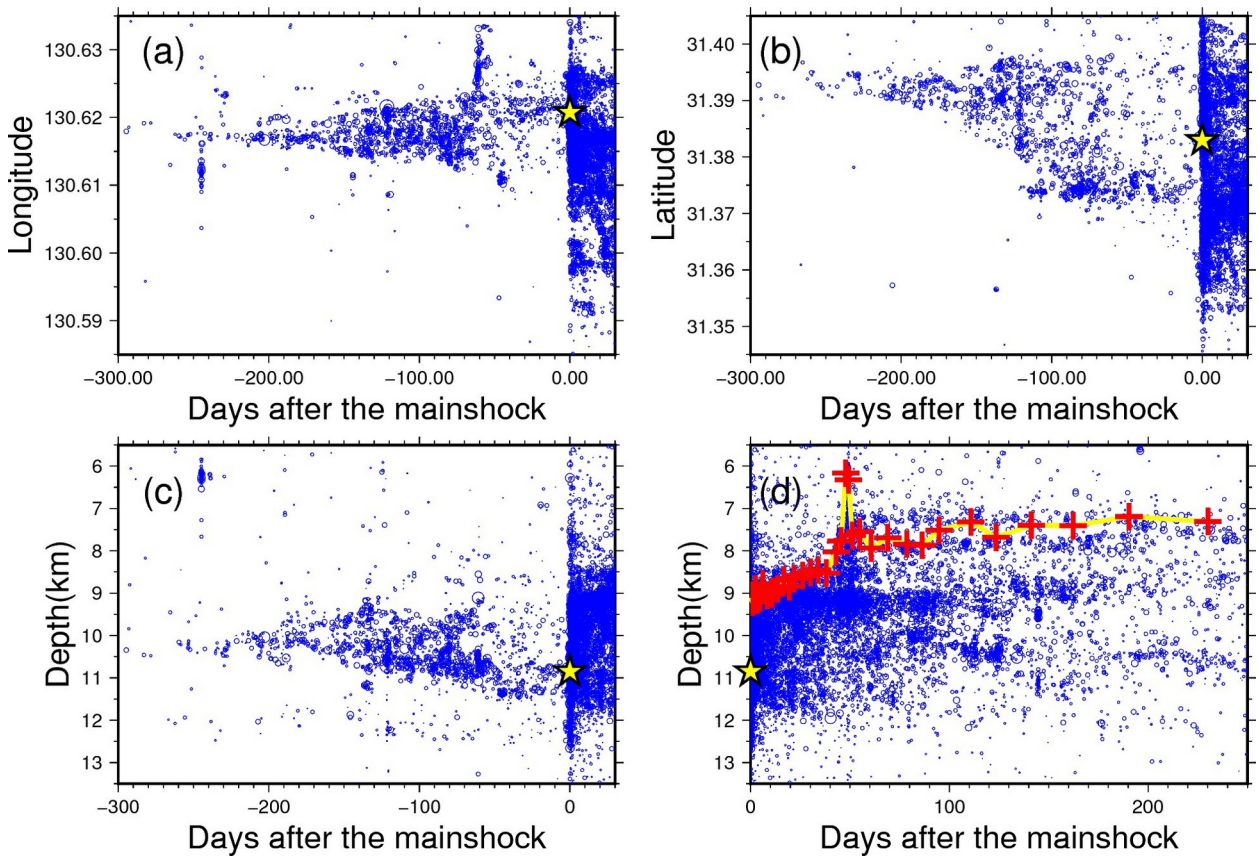
(a)
Longitude
130.63
130.62
130.61
130.60
130.59
−300.00
−200.00
−100.00
0.00
Days after the mainshock
(b)
Latitude
31.40
31.39
31.38
31.37
31.36
31.35
−300.00
−200.00
−100.00
0.00
Days after the mainshock
(c)
Depth(km)
6
7
8
9
10
11
12
13
−300
−200
−100
0
Days after the mainshock
(d)
Depth(km)
6
7
8
9
10
11
12
13
0
100
200
Days after the mainshock

394

395 **Figure 8.** Temporal evolution of hypocenters in the (**a**) latitude, (**b)** longitude, and (**c**) depth
396 directions. (**d**) Temporal evolution of the aftershock hypocenters in the depth direction. The red
397 crosses and yellow curve in (**d**) indicate the depth above which the shallowest 10% of the
398 hypocenters are located (D10) for every bin with 400 events based on the occurrence time. The
399 circle size corresponds to the JMA magnitude. The yellow star indicates the hypocenter of the
400 mainshock.
401

402 Figures 7d–f show the distribution of aftershock hypocenters colored based on the
403 occurrence time of each event. Figure 8d shows the temporal evolution of the aftershock
404 hypocenters as a function of the depth. The temporal evolution of the aftershock hypocenters in
405 both the latitudinal and longitudinal directions is shown in Fig. S7. Because the spatial
406 distribution of the aftershocks is complex, the spatiotemporal features of the aftershocks are
407 more difficult to determine than those of the foreshocks. Overall, the aftershock hypocenters
408 move upward with time, as shown in Fig. 8d, which depicts the depths above which the
409 shallowest 10% of the hypocenters are located (D10) for each bin containing 400 events, as
410 denoted by the red curve. Although earthquakes occur in a relatively deep region immediately
411 after the mainshock, the upper limit of the seismic depth (D10) gradually moves in the shallow
412 direction, that is, the hypocenters gradually move to the shallower part with time after the
413 mainshock.
414

415 **3.3 Deviation of the seismicity from Omori's law**

416 We investigated the seismicity rate of the Kagoshima Bay earthquake sequence after the
417 mainshock. Figure 1d shows the seismicity rates of the $M_{JMA} \geq 1.0$ events in the area surrounding

the hypocenter of the mainshock (red frame in Fig. 1b). The seismic rate was obtained by calculating the reciprocal of the time required to generate ten earthquakes that were arranged in chronological order. Based on Fig. 1d, the seismicity rate decreases by the power of the elapsed time immediately after the mainshock, as described by the modified Omori law (Utsu, 1961). The seismicity rate abruptly increases ~44 days after the mainshock, which corresponds to the occurrence of the largest aftershock ($M_L$ 4.4), suggesting that the increase is due to secondary aftershocks. A period with a high seismicity rate started approximately 20 to 40 days after the mainshock; the seismic activity was temporarily strong despite the absence of large aftershocks.

Based on maximum likelihood estimation, we obtained the following parameters for the ETAS model: $K_0 = 34.205$, $c = 1.3163 \times 10^{-2}$, $p = 1.0685$, $\alpha = 1.5078$, and $\mu = 2.9603 \times 10^{-2}$. Based on Ogata (1992), the range of α-values is 0.35–0.85 for swarm seismicity and 1.2– 3.1 for non-swarm seismicity. The α value estimated for the seismic activity in Kagoshima Bay is within the latter range.

In Fig. 9, the cumulative number of earthquakes simulated using the estimated model parameters is compared with the observations. Overall, the number predicted based on the ETAS model matches the observations. However, the simulated number of earthquakes is lower than the observed number 20–40 days after the mainshock. To quantitatively examine the magnitude of the discrepancy between the model and observations, we performed residual analysis using the transformed time, similar to Ogata (1988). Figure 9c shows that the discrepancy between the model and observations is high at a transformed time between 1.000 and 1.500, corresponding to the period of 20–40 days after the mainshock. This deviation is significant at the 95% significance level based on the assumption of a uniform distribution.

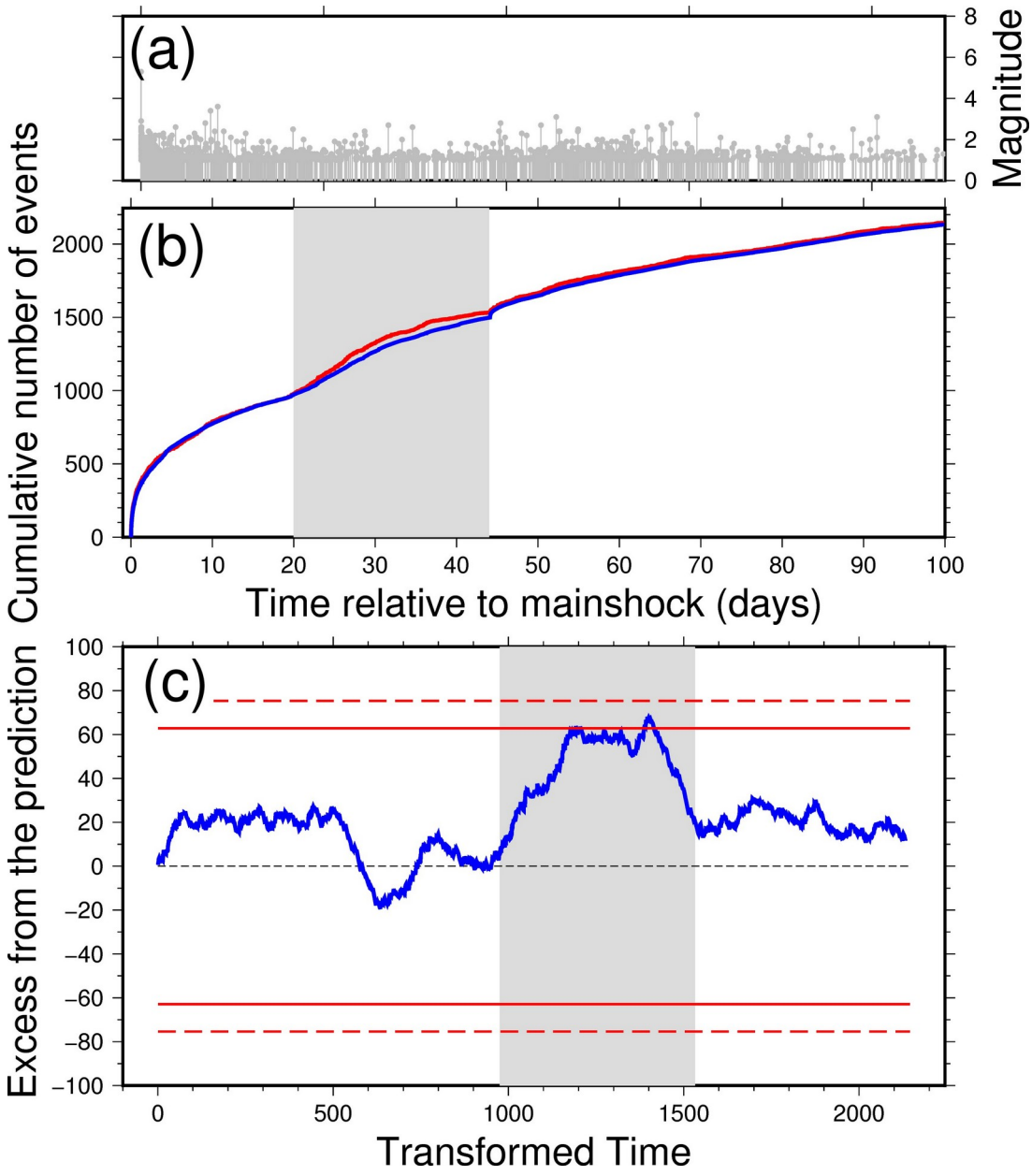


441

442 **Figure 9.** (**a**) M–T diagram. (**b**) Observed cumulative number of aftershocks with $M_L \geq 1.0$ (red
443 solid line) and predicted number based on the estimated ETAS parameters (blue solid line). Each
444 curve represents the cumulative numbers starting 0.1 days after the mainshock. (**c**) Results of the
445 residual analysis, where the blue solid line shows the observed events with respect to the
446 transformed time on the horizontal axis and cumulative number of observed $M_L \geq 1.0$
447 earthquakes on the vertical axis. The black dotted line represents the transformed time at which

the assumed model fully matches the observation. The red solid and red broken lines indicate the two-sided 95% and 99% error bounds of the Kolmogorov–Smirnov statistic, respectively. The gray zone in (**c**) shows the range of the transformed time corresponding to the period of 20–44 days after the mainshock highlighted in gray in (**b**).

The large discrepancy between the predicted and observed seismicity rates 20–40 days (~1.000–1.500 in Fig. 9c) after the mainshock can be explained by a temporary increase in the background seismicity, which was assumed to be constant over the entire period of this analysis in the model. The transient increase in the background seismicity rate suggests that the Kagoshima Bay earthquake sequence may have been affected by physical processes other than earthquake-to-earthquake interactions, especially during this period (20–40 days) and that an aseismic process may have led to the largest aftershock ($M_L$ 4.4) that occurred 44 days after the mainshock. Contrarily, most aftershocks can be explained as general mainshock–aftershock seismic activity, suggesting that stress changes caused by the mainshock resulted in numerous aftershocks.

## 4 Discussion

Our results show that: (1) the foreshocks of the 2017 M5.3 Kagoshima Bay earthquake sequence occurred on a single plane with a steep dip to the east, whereas aftershocks occurred on several more complex planar structures, (2) the foreshock hypocenters formed a seismic gap, and (3) the foreshock and aftershock hypocenters exhibit clear migration behaviors. In this section, we integrated these observations and propose a simple model that can explain the occurrence of the foreshock–mainshock–aftershock sequence of the 2017 M5.3 Kagoshima Bay earthquake based on the upward fluid movement, which is similar to the fault-valve model proposed by Sibson (1992).

### 4.1 Migration of foreshock activity along a plane

The clear hypocenter migration observed for the foreshock sequence suggests that aseismic physical processes controlled this sequence. In fact, the seismicity rate of the foreshock sequence could not be reproduced by the ETAS model, suggesting that the earthquake-to-earthquake interaction cannot explain this sequence. Thus, the foreshock sequence must be understood as temporary increase in the background seismicity rate, similar to that of the earthquake swarm.

In Fig. 10, the distances of the foreshock hypocenters from the mean location of the first three events are plotted against time. The expansion front of the pore pressure diffusion model reported in Shapiro et al. (1997) is also shown, which can be expressed by the following equation including various diffusion coefficients $D_h$:

$$r = \sqrt{4 \pi D_h t}, \quad (9)$$

where $r$ is the distance from the point pressure source and $t$ is the time. In this study, we set the initiation time to 220 days before the mainshock because the seismicity rate significantly

increased at this time (Fig. 1c). We also show the propagation fronts of the linear spread model that has been used for aseismic slip propagation in the past (e.g., Vidale & Shearer, 2006).

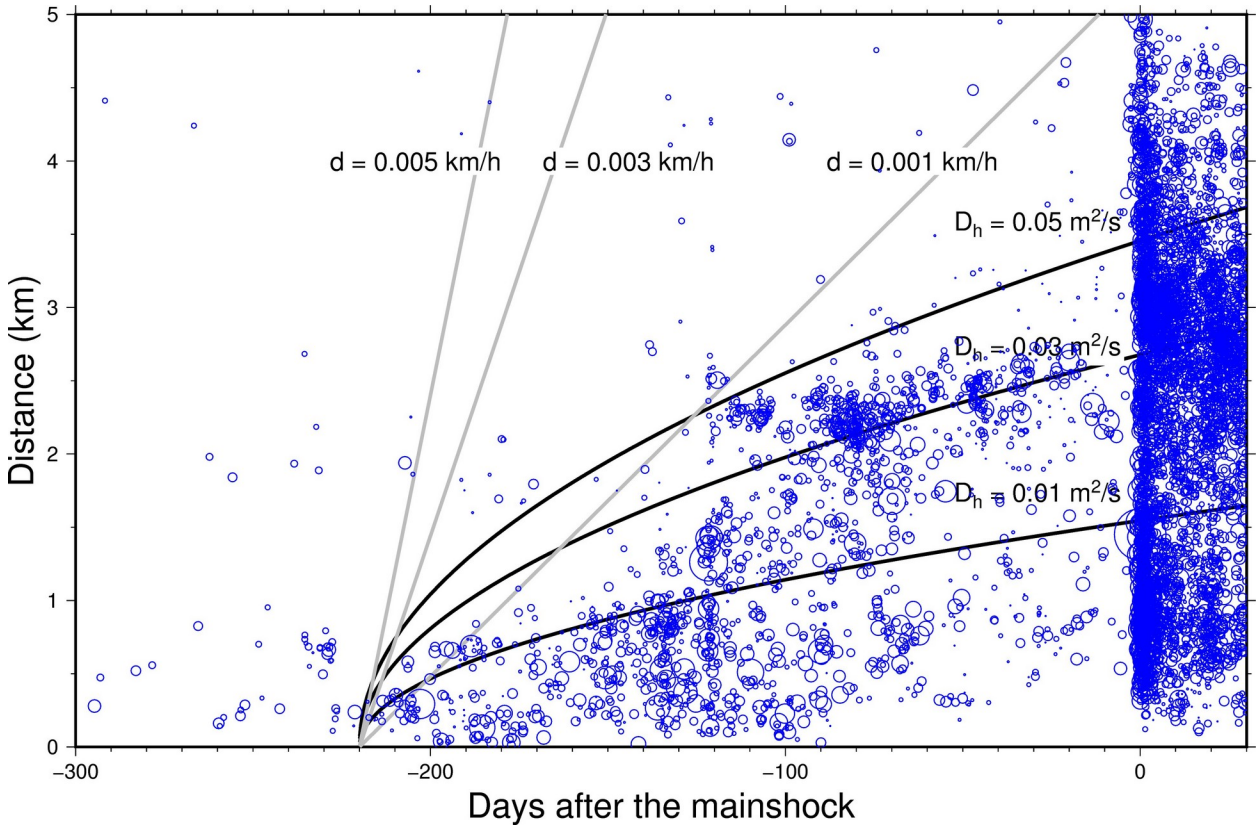


**Figure 10.** Temporal evolution of the distances between the foreshocks and initial hypocenter. Blue circles represent the hypocenters expressed by the size corresponding to the JMA magnitude. The black curves show the fluid diffusion models with $D_h$ = 0.01, 0.03, and 0.05 $m^2/s$. Gray straight lines show the linear spread model with migration speeds of d = 0.001, 0.003, and 0.005 km/h.

The pore pressure diffusion model with a hydraulic diffusion coefficient of ~0.05 $m^2/s$ matches the observations better than the linear spread model. In previous studies, it has been

estimated that the hydraulic diffusion coefficient in the crust ranges from ~0.01–10 $m^2/s$ (e.g., Talwani et al., 2007; Shelly et al., 2016; Yoshida & Hasegawa, 2018a), which is similar to the foreshock migration speed of the M5.3 Kagoshima Bay earthquake sequence. Based on the linear spread model, the propagation velocity is ~0.001–0.005 km/h. Based on previous studies, the migration speed of aseismic slip propagation ranges from 0.1–1.0 km/h (e.g., Lohman & McGuire, 2007; Kato et al., 2016), which is significantly higher than the migration speed of the present foreshock activity. If we advance the initiation timing of propagation, the propagation speed decreases. Thus, according to the migration speed and spatiotemporal pattern of the foreshocks, the pore pressure diffusion model better explains the overall migration of the foreshock hypocenters.

Aseismic creep related to the nucleation process of the mainshock might be involved in the migration of the foreshocks. In fact, physical simulations indicate interseismic creep in seismogenic patches from external stable-slip regions before the occurrence of unstable slip (Tse & Rice, 1986). Such an expansion of quasi-static slip prior to the mainshock may explain the current migration of the foreshocks (e.g., Dodge et al., 1996; Yabe & Ide, 2018). However, the source of the mainshock is smaller than the foreshock area (Fig. 6a), which contradicts the hypothesis because the mainshock rupture zone should include the nucleation area. Note that the size of the source of the mainshock was estimated based on source models assuming a constant rupture velocity (subshear rupture propagation). If the assumptions differ from reality (e.g., supershear rupture propagation), the source size may differ from our estimation, explaining this contradiction. However, the aftershocks migrate upward on multiple planes (Fig. 8d), which can be explained with the foreshock sequence if the pore pressure migration model is adopted. Thus, we prefer the hypothesis that pore pressure migration is primarily responsible for the generation

523 of the 2017 M5.3 Kagoshima Bay earthquake sequence. The heterogeneity in the permeability
524 and/or pore pressure along the fault may explain the up- and downward movement of the
525 hypocenter along the plane (Fig. 8c).

526 However, recent observations of fluid injection-induced seismicity and natural earthquake
527 swarms suggest that an increase in the pore pressure can cause aseismic slip (Cornet et al., 1997;
528 Guglielmi et al., 2015; Ruhl et al., 2016; Yoshida & Hasegawa, 2018a; De Barros et al., 2020). In
529 the presence of fluids, the effective normal stress decreases and the critical nucleation size
530 increases; thus, the occurrence of aseismic slip is likely (e.g., Scholz, 1998). The increase in the
531 pore pressure also accelerates creep in the stable-slip segment of the fault. Both aseismic slip and
532 fluid movement may have contributed to the occurrence of foreshocks. Furthermore, the
533 poroelastic effects associated with pore pressure migration (Segall, 1989; Goebel et al., 2018)
534 and the earthquake-to-earthquake interaction (Helmstetter, 2002) may contribute to the
535 occurrence of earthquakes.

536

537 **4.2 Seismic gap of the foreshock and aftershock sequence in the mainshock fault plane**

538 The doughnut-like pattern of the foreshocks (Fig. 6) is similar to the "Mogi doughnut" (Mogi,
539 1969). It has been reported that aftershocks do not occur in the mainshock region (e.g., Mendoza
540 & Hartzell, 1988; Das & Henry, 2003; Woessner et al., 2006; Asano et al., 2011; Ebel &
541 Chambers, 2016; Yoshida et al., 2016b and 2020a; Ross, 2017b, 2018; Wetzler et al., 2018),
542 which is likely because the shear stress was released during the mainshock. In Figure 6a, the size
543 of the seismic gap is compared with the estimated size of the fault related to the mainshock.
544 Because the centroid location of the mainshock was not determined, we assumed the centroid is
545 located by a few hundred meters into the shallower region such that the mainshock centroid is

546 located in the center of the seismic gap shown in the figure. The fault size of the mainshock is
547 similar to that of the seismic gap. This is consistent with the hypothesis that the mainshock
548 rupture occurred in the seismic gap of the foreshock and aftershock activities. A similar spatial
549 separation of the mainshock and fore- and aftershocks in the rupture area was also reported for a
550 recent M5.2 intraplate earthquake that occurred in Akita, NE Japan (Yoshida et al., 2020).

551 The seismic gap in the foreshock activity may originate from the spatial heterogeneities in
552 the frictional and material properties along the fault plane. The fault strength of the mainshock
553 rupture area may have been higher than that of the surrounding area, as proposed in the asperity
554 model of Lay & Kanamori (1981). Foreshocks can be understood as failures of small
555 seismogenic patches in the surrounding stable area. Alternatively, the area may have been
556 covered by an impermeable medium, hindering fluid intrusion. The occurrences of foreshocks
557 and aseismic slip increased the shear stress in the future source region of the mainshock rupture.
558 The mainshock occurred in this region due to the gradually increasing pore pressure and shear
559 stress.

560

561 **4.3 Upward migration of the aftershocks along several planes**

562 The aftershock sequence of the Kagoshima Bay earthquake sequence follows Omori's law
563 (Fig. 1d), suggesting that this sequence was triggered by the M5.3 mainshock. However, the
564 aftershock sequence slightly deviates from the prediction based on the ETAS model (Figs 9b–c).
565 The transient increase in the background seismicity rate suggests that the Kagoshima Bay
566 earthquake sequence may have been affected by physical processes other than earthquake-to-
567 earthquake interactions, especially during this period (20 to 40 days) and that these aseismic
568 processes may have led to the largest aftershock ($M_L$ 4.4) that occurred 44 days after the

569 mainshock. Based on the model simulations of fluid injection-induced seismicity, Hainzl and
570 Ogata (2005) pointed out that the background seismicity rate of the ETAS model is sensitive to
571 the amount of injected water. In previous studies, similar observations were made for fluid
572 injection-induced seismicity and natural earthquake sequences (Llenos & Michael, 2013;
573 Yoshida & Hasegawa, 2018b; Kumazawa et al., 2019).

574 Our results indicate that the aftershock hypocenters migrated toward the shallower portion
575 on multiple planes. Such upward movements of hypocenters have been previously reported for
576 earthquake swarms following nearby large earthquakes and it has been concluded that they
577 reflect the upward pore pressure migration associated with the fault-valve behavior (Shelly et al.,
578 2015; Ruhl et al., 2016; Yoshida & Hasegawa, 2018a, b). Examples are the earthquake swarms
579 that occurred in northeastern Japan following the 2011 Tohoku-Oki earthquake (Yoshida et al.,
580 2016a; Yoshida & Hasegawa, 2018a, b). The earthquake swarms might originate from the pore
581 pressure increase because (1) they occurred in the stress shadow of the 2011 Tohoku-Oki
582 earthquake with a time delay of a few weeks despite the reduction in the shear stress, (2) they are
583 located beneath the caldera structures that are believed to host shallow igneous bodies, with
584 hydrothermal fluids immediately below, (3) they are located a few kilometers above S-wave
585 reflectors and the low-velocity zone including fluids, and (4) their hypocenters migrate upward
586 (Yoshida & Hasegawa, 2018a; Yoshida et al., 2019a). The Kagoshima Bay swarm was also
587 located beneath an ancient caldera and involved the upward migration of aftershocks, which can
588 be explained by an increase in the pore pressure. Fluid paths in the crust may have expanded due
589 to the deformation and shaking associated with the mainshock. Pore pressure migration may
590 explain deviations in the seismicity rate from Omori's law. These observations are consistent
591 with the prediction based on the fault-valve model proposed in Sibson (1992), that is, upward

fluid discharge after the mainshock. In recent geodetic studies, a porosity wave associated with the fault-valve action was detected (Rossi et al., 2016 and 2018).

We presume that the subducting Philippine Sea Plate is the source of fluids, similar to the model reported in Hasegawa et al. (2005), which is based on the geophysical and geological observations in northeastern Japan. This hypothesis is supported by seismic data obtained in Kyushu using tomography, which indicate that the existence of an inclined low-velocity layer continuously distributed in the mantle wedge and reaching right below the volcanic front as northeastern Japan (Zhao et al., 2012). The low-velocity zone is considered to represent the ascending flow portion of the secondary convection within the mantle wedge and therefore contains fluids from the slab and resultant melts (Hasegawa et al., 2005). The buoyancy facilitated the upward migration of the fluids, as shown in simulations (e.g., Iwamori, 1998; Wada et al., 2015; Horiuchi et al., 2016), and the fluids reached the source region of the Kagoshima Bay sequence.

### 4.4 Comprehensive interpretation of the seismic activity in Kagoshima Bay

Here, we summarize our simple model that comprehensively explains the observed results of the foreshock-mainshock-aftershock sequence of the 2017 M5.3 Kagoshima Bay earthquake.

First, fluids that have infiltrated the mainshock fault plane caused the foreshock activity. The hypocenter migration of the foreshock activity can be interpreted considered to be a reflection of fluid movement and possibly triggered aseismic slip on the plane. Second, the occurrences of foreshocks and aseismic slip increased the shear stress in the future source region of the mainshock (seismic gap in Fig. 6). The mainshock finally occurred in this region due to the gradually increasing pore pressure and shear stress. Third, the change in the stress associated

with the occurrence of the mainshock primarily triggered aftershocks in the area surrounding the mainshock including regions outside the mainshock fault plane. Fluids started to move upward due to the deformation and shaking associated with the mainshock. Together with the fluids, the aftershock hypocenters moved to shallower regions. Thus, the overall sequence of the 2017 M5.3 Kagoshima Bay earthquake can be explained by consistent upward fluid movement.

### 4.5 Implications to the foreshock–mainshock–aftershock sequence

The results of previous studies suggested that many earthquake swarms are caused by the movements of crustal fluids (e.g., Mogi, 1989; Italiano et al., 2001; Fischer and Horálek, 2003; Parotidis et al., 2003; Bianco et al., 2004; Yukutake et al., 2011; Shelly et al., 2016; Yoshida et al., 2016a; Ruhl et al., 2016; De Barros et al., 2019). The results of the present study suggest that the generation mechanism of the foreshock activity is the same as that of earthquake swarms, that is, a temporary increase in background seismicity rate due to increasing pore pressure and aseismic slip. The whole sequence of the Kagoshima Bay seismicity can be understood as the transition from swarm activity to the mainshock–aftershock sequence.

The 2008 Mogul earthquake swarm, Nevada, may be a similar example. This sequence was also initiated by swarm activity but shifted to a mainshock–aftershock sequence after the occurrence of the M4.9 mainshock. The upward migration of the earthquakes suggests that fault-valve behavior is involved in the occurrence of this earthquake sequence (Ruhl et al., 2016). The aftershock activities of the 2014 $M_L$ 4.8, Ubaye earthquake, France (De Barros et al., 2019), and the foreshock and aftershock activities of the 2017 M5.2 Akita-Daisen event can also be understood as transitions from swarm activity to mainshock–aftershock sequences (Yoshida et al., 2020b). Similarly, aseismic slip may have caused the foreshocks and mainshock of the 2011

638 M9 Tohoku-Oki earthquake (Kato et al., 2012); 2014 Iquique Mw 8.1 earthquake, Chile (Kato &
639 Nakagawa, 2014); and 2009 M6.3 L'Aquila earthquake (Borghi et al., 2016). It is likely that pore
640 pressure migration and aseismic slip propagation occasionally coexist (Waite & Smith, 2002;
641 Ross et al., 2017a; Yoshida & Hasegawa, 2018; De Barros et al., 2020) and contribute to the
642 increase in the background seismicity rate. Such aseismic processes may also cause mainshock–
643 aftershock activity without notable foreshocks. The 2019 M6.7 Yamagata-Oki earthquake, NE
644 Japan, may be an example. The earthquake occurred in the stress shadow of the 2011 Tohoku-
645 Oki earthquake and exhibited an upward aftershock migration (Yoshida et al., 2020b). These
646 observations suggest that the monitoring of aseismic processes is crucial to understanding the
647 seismic activity.

648

## 5 Conclusions

The results of previous studies suggested that many earthquake swarms have been caused by the movement of crustal fluids (e.g., Mogi, 1989; Fischer and Horálek, 2003; Parotidis et al., 2003; Bianco et al., 2004; Yukutake et al., 2011; Chen et al., 2012; Shelly et al., 2016; Yoshida et al., 2016a; Ruhl et al., 2016; De Barros et al., 2019). In the present study, the intense foreshock–mainshock–aftershock sequence of the 2017 M5.3 Kagoshima Bay earthquake was examined. The results show that the whole sequence can be explained by upward fluid movement: (1) most foreshocks were located on a single plane with a steep dip to the east and migrated along the plane. This foreshock migration can be interpreted as a reflection of fluid movement and possibly triggered aseismic slip on the plane; (2) The hypocenter of the mainshock was located at the edge of a seismic gap with a size comparable to that of the source of the mainshock rupture. This suggests that the mainshock rupture was due to the slip of this seismic gap and the seismic gap was a large seismogenic patch with higher fault strength, which finally ruptured due to the increase in the pore pressure and aseismic slip in the surrounding areas; and (3) Aftershocks occurred on several planes with a steep dip to the east and moved from deeper to shallower regions. The upward migration can be interpreted as a reflection of post-failure fluid discharge. Thus, the overall sequence of the 2017 M5.3 Kagoshima Bay earthquake can be explained by upward fluid movement, as presumed by the fault-valve model (Sibson, 1992).

The whole sequence of the Kagoshima Bay seismicity can be understood as the transition from swarm activity to a mainshock–aftershock sequence. The results of the present study suggest that the generation mechanism of the foreshock activity is the same as that of the earthquake swarms, that is, a temporary increase in the background seismicity rate due to increasing pore pressure and aseismic slip. Aseismic processes sometimes cause a large

672 earthquakes that is followed by numerous aftershocks; the foreshock–mainshock–aftershock
673 sequence may such a sequence.
674

675 **Acknowledgments**

676 We thank the editor Rachel Abercrombie, Giuliana Rossi, and an anonymous reviewer for
677 their constructive comments, which improved the manuscript. KY thanks Dapeng Zhao for the
678 information of seismic velocity structure in Kyushu. In this study, hypocenter and P- and S-
679 wave data reported in the unified catalog of the JMA (https://www.data.jma.go.jp/svd/eqev/data/
680 bulletin/index_e.html) were used. The seismograms were collected and stored by the JMA,
681 National Universities, and National Research Institute for Earth Science and Disaster Resilience
682 (http://www.hinet.bosai.go.jp/?LANG=en). The figures in this paper were created using GMT
683 (Wessel & Smith, 1998). This research was supported by JSPS KAKENHI Grant Number JP
684 17K1437. The results obtained for the hypocenters, focal mechanisms, and coseismic slip
685 distribution are available at http://www.aob.gp.tohoku.ac.jp/~yoshida/pub/JGR2020b/.
686

## References

Aki, K. (1965). A computer program for precise determination of focal mechanism of local earthquakes by revising focal depths and crust-mantle structure. *Bulletin of the Earthquake Research Institute*, *43*, 15–22.

Aki, K. (1967). Scaling law of seismic spectrum. *Journal of Geophysical Research*, *72*(4), 1217–1231. https://doi.org/10.1029/JZ072i004p01217

Asano, Y., Saito, T., Ito, Y., Shiomi, K., Hirose, H., Matsumoto, T., . . . Sekiguchi, S. (2011). Spatial distribution and focal mechanisms of aftershocks of the 2011 off the Pacific coast of Tohoku Earthquake. *Earth, Planets and Space*, *63*(7), 669–673. https://doi.org/10.5047/eps.2011.06.016

Bianco, F., Del Pezzo, E., Saccorotti, G., & Ventura, G. (2004). The role of hydrothermal fluids in triggering the July-August 2000 seismic swarm at Campi Flegrei, Italy: Evidence from seismological and mesostructural data. *Journal of Volcanology and Geothermal Research*, *133*(1–4), 229–246. https://doi.org/10.1016/S0377-0273(03)00400-1

Borghi, A., Aoudia, A., Javed, F., & Barzaghi, R. (2016). Precursory slow-slip loaded the 2009 L'Aquila earthquake sequence. *Geophysical Journal International*, *205*(2), 776–784. https://doi.org/10.1093/gji/ggw046

Brune, J. N. (1970). Tectonic stress and the spectra of seismic shear waves from earthquakes. *Journal of Geophysical Research*, *75*(26), 4997–5009. https://doi.org/10.1029/JB075i026p04997

Cornet, F. H., Helm, J., Poitrenaud, H., & Etchecopar, A. (1997). Seismic and aseismic slips induced by large-scale fluid injections. In. *Pure and Applied Geophysics*. Berlin: Springer, 150(3–4), (563–583). https://doi.org/10.1007/s000240050093

Cox, S. F. (2016). Injection-driven swarm seismicity and permeability enhancement: Implications for the dynamics of hydrothermal ore systems in high fluid-flux, overpressured faulting regimes–an invited paper. *Economic Geology*, *111*(3), 559–587. https://doi.org/10.2113/econgeo.111.3.559

Dahm, T. (1996). Relative moment tensor inversion based on ray theory: Theory and synthetic tests. *Geophysical Journal International*, *124*(1), 245–257. https://doi.org/10.1111/j.1365-246X.1996.tb06368.x

Das, S., & Henry, C. (2003). Spatial relation between main earthquake slip and its aftershock distribution. *Reviews of Geophysics*, *41*(3). https://doi.org/10.1029/2002RG000119

De Barros, L., Baques, M., Godano, M., Helmstetter, A., Deschamps, A., Larroque, C., & Courboulex, F. (2019). Fluid-Induced Swarms and Coseismic Stress Transfer: A Dual Process Highlighted in the Aftershock Sequence of the 7 April 2014 Earthquake (Ml 4.8, Ubaye, France). *Journal of Geophysical Research: Solid Earth*, *124*(4), 3918–3932. https://doi.org/10.1029/2018JB017226

De Barros, L., Cappa, F., Deschamps, A., & Dublanchet, P. (2020). Imbricated aseismic slip and fluid diffusion drive a seismic swarm in the Corinth Gulf, Greece. *Geophysical Research Letters*, 47(9). https://doi.org/10.1029/2020GL087142

Dodge, D. A., Beroza, G. C., & Ellsworth, W. L. (1996). Detailed observations of California foreshock sequences: Implications for the earthquake initiation process. *Journal of Geophysical Research: Solid Earth*, *101*(B10), 22371–22392. https://doi.org/10.1029/96JB02269

731 Ebel, J. E., & Chambers, D. W. (2016). Using the locations of M ≥ 4 earthquakes to delineate the
732 extents of the ruptures of past major earthquakes. *Geophysical Journal International*,
733 *207*(2), 862–875. https://doi.org/10.1093/gji/ggw312
734 Ellsworth, W. L. (2013). Injection-induced earthquakes. *Science*, *341*(6142), 1225942.
735 https://doi.org/10.1126/science.1225942
736 Fischer, T., & Horálek, J. (2003). Space-time distribution of earthquake swarms in the principal
737 focal zone of the NW Bohemia/Vogtland seismoactive region: Period 1985-2001. *Journal*
738 *of Geodynamics*, *35*(1–2), 125–144. https://doi.org/10.1016/S0264-3707(02)00058-3
739 Goebel, T. H. W., Weingarten, M., Chen, X., Haffener, J., & Brodsky, E. E. (2017). The 2016
740 Mw5.1 Fairview, Oklahoma earthquakes: Evidence for long-range poroelastic triggering at
741 >40 km from fluid disposal wells. *Earth and Planetary Science Letters*, *472*, 50–61.
742 https://doi.org/10.1016/j.epsl.2017.05.011
743 Guglielmi, Y., Cappa, F., Avouac, J. P., Henry, P., & Elsworth, D. (2015). INDUCED
744 SEISMICITY. Seismicity triggered by fluid injection-induced aseismic slip. *Science*,
745 *348*(6240), 1224–1226. https://doi.org/10.1126/science.aab0476
746 Gutenberg, B., & Richter, C. F. (1944). Frequency of earthquakes in California. *Bulletin of the*
747 *Seismological Society of America*, *34*(4), 185–188.
748 Hainzl, S., & Ogata, Y. (2005). Detecting fluid signals in seismicity data through statistical
749 earthquake modeling. *Journal of Geophysical Research*, *110*(B5), 1–10.
750 https://doi.org/10.1029/2004JB003247
751 Hasegawa, A. (2017). Role of $H_2O$ in generating subduction zone earthquakes. *Monographs on*
752 *Environment, Earth and Planets*, *5*(1), 1–34.
753 https://doi.org/10.5047/meep.2017.00501.0001

754 Hasegawa, A., Nakajima, J., Umino, N., & Miura, S. (2005). Deep structure of the northeastern
755 Japan arc and its implications for crustal deformation and shallow seismic activity.
756 *Tectonophysics*, *403*(1–4), 59–75. https://doi.org/10.1016/j.tecto.2005.03.018
757 Helmstetter, A., & Sornette, D. (2002). Diffusion of epicenters of earthquake aftershocks,
758 Omori's law, and generalized continuous-time random walk models. *Physical Review E -*
759 *Statistical Physics, Plasmas, Fluids, and Related Interdisciplinary Topics*, *66*(6), 24.
760 https://doi.org/10.1103/PhysRevE.66.061104
761 Horiuchi, S. S., & Iwamori, H. (2016). A consistent model for fluid distribution, viscosity
762 distribution, and flow-thermal structure in subduction zone. *Journal of Geophysical*
763 *Research: Solid Earth*, *121*(5), 3238–3260. https://doi.org/10.1002/2015JB012384
764 Hubbert, M. K., & Rubey, W. W. (1959). *Role of fluid overpressure in the mechanics of*
765 *overthrust faulting [Geological Society of America bulletin]*, *70* (pp. 167–206).
766 https://doi.org/10.1130/0016-7606(1959)70
767 Imanishi, K., & Ellsworth, W. L. (2006). Source scaling relationships of microearthquakes at
768 Parkfield, CA, determined using the SAFOD pilot hole seismic array *[Geophysical*
769 *monograph series]*. *Geophysical Monograph Series*, 81–90.
770 https://doi.org/10.1029/170GM10
771 Italiano, F., Martinelli, G., & Nuccio, P. M. (2001). Anomalies of mantle-derived helium during
772 the 1997-1998 seismic swarm of Umbria-Marche, Italy. *Geophysical Research Letters*,
773 *28*(5), 839–842. https://doi.org/10.1029/2000GL012059
774 Iwamori, H. (1998). Transportation of H2O and melting in subduction zones. *Earth and*
775 *Planetary Science Letters*, *160*(1–2), 65–80. https://doi.org/10.1016/S0012-
776 821X(98)00080-6

Kaneko, Y., & Shearer, P. M. (2014). Seismic source spectra and estimated stress drop derived from cohesive-zone models of circular subshear rupture. *Geophysical Journal International*, *197*(2), 1002–1015. https://doi.org/10.1093/gji/ggu030

Kato, A., Obara, K., Igarashi, T., Tsuruoka, H., Nakagawa, S., & Hirata, N. (2012). Propagation of Slow Slip Leading Up to the 2011 Mw 9.0 Tohoku-Oki Earthquake. *Science*, *335*(6069), 705–708. https://doi.org/10.1126/science.1215141

Kato, A., & Nakagawa, S. (2014). Multiple slow-slip events during a foreshock sequence of the 2014 Iquique, Chile Mw 8.1 earthquake. *Geophysical Research Letters*, *41*(15), 5420–5427.

Kato, A., Fukuda, J., Nakagawa, S., & Obara, K. (2016). Foreshock migration preceding the 2016 MW 7.0 Kumamoto earthquake, Japan. *Geophysical Research Letters*, *43*(17), 8945–8953. https://doi.org/10.1002/2016GL070079

Kumazawa, T., & Ogata, Y. (2013). Quantitative description of induced seismic activity before and after the 2011 Tohoku-Oki earthquake by nonstationary ETAS models. *Journal of Geophysical Research: Solid Earth*, *118*(12), 6165–6182. https://doi.org/10.1002/2013JB010259

Kumazawa, T., Ogata, Y., & Tsuruoka, H. (2019). Characteristics of seismic activity before and after the 2018 M6. 7 Hokkaido Eastern Iburi earthquake. *Earth, Planets and Space*, *71*(1), 1–17.

Lay, T., & Kanamori, H. (1981). An asperity model of large earthquake sequences. In. *Maurice Ewing Series*. Maurice Ewing Series. American Geophysical Union, (579–592). https://doi.org/10.1029/ME004p0579

799 Llenos, A. L., & Michael, A. J. (2013). Modeling earthquake rate changes in Oklahoma and
800 Arkansas: Possible Signatures of induced seismicity. *Bulletin of the Seismological Society*
801 *of America*, *103*(5), 2850–2861. https://doi.org/10.1785/0120130017
802 Lohman, R. B., & McGuire, J. J. (2007). Earthquake swarms driven by aseismic creep in the
803 Salton Trough, California. *Journal of Geophysical Research: Solid Earth*, 112(B4). https://
804 doi.org/10.1029/2006JB004596
805 Madariaga, B. Y. R. (1976). Dynamics of an expanding circular fault. *Bulletin of the*
806 *Seismological Society of America*, *66*, 639–666. https://doi.org/10.1111/j.1461-
807 0248.2009.01352.x
808 Mendoza, C., & Hartzell, S. H. (1988). Aftershock patterns and main shock faulting. *Bulletin of*
809 *the Seismological Society of America*, *78*(4), 1438–1449.
810 Mogi, K. (1969). Some features of recent seismic activity in and near Japan (2): Activity before
811 and after Great Earthquakes. *Bulletin of the Earthquake Research Institute*, *47*, 395–417.
812 Mogi, K. (1989). The mechanism of the occurrence of the Matsushiro earthquake swarm in
813 central Japan and its relation to the 1964 Niigata earthquake. Tectonophysics, 159(1–2),
814 109–119.
815 Nanjo, K. Z., Miyaoka, K., Tamaribuchi, K., Kobayashi, A., & Yoshida, A. (2018). Related
816 spatio-temporal changes in hypocenters and the b value in the 2017 Kagoshima Bay
817 swarm activity indicating a rise of hot fluids. *Tectonophysics*, *749*, 35–45.
818 https://doi.org/10.1016/j.tecto.2018.10.023
819 Nur, A., & Booker, J. R. (1972). Aftershocks caused by pore fluid flow? *Science*, *175*(4024),
820 885–887. https://doi.org/10.1126/science.175.4024.885

Ogata, Y. (1988). Statistical models for earthquake occurrences and residual analysis for point processes. *Journal of the American Statistical Association*, *83*(401), 9–27. https://doi.org/10.1080/01621459.1988.10478560

Ogata, Y. (1992). Detection of precursory relative quiescence before great earthquakes through a statistical model. *Journal of Geophysical Research*, *97*(B13), 19845–19871. https://doi.org/10.1029/92JB00708

Ogata, Y. (2006). *Statistical analysis of seismicity: Updated version* (p. SASeis2006). Institute of Statistical Mathematics.

Okada, T., Matsuzawa, T., Umino, N., Yoshida, K., Hasegawa, A., Takahashi, H. et al. (2016). Hypocenter migration and crustal seismic velocity distribution observed for the inland earthquake swarms induced by the 2011 Tohoku-Oki earthquake in NE Japan: Implications for crustal fluid distribution and crustal permeability. In *Crustal Permeability*, (307–323). https://doi.org/10.1002/9781119166573.ch24

Parotidis, M., Rothert, E., & Shapiro, S. A. (2003). Pore-pressure diffusion: A possible triggering mechanism for the earthquake swarms 2000 in Vogtland/NW-Bohemia, central Europe. Geophysical Research Letters, 30(20), 10–13. https://doi.org/10.1029/2003GL018110

Prieto, G. A., Parker, R. L., & Vernon III, F. L. (2009). A Fortran 90 library for multitaper spectrum analysis. *Computers and Geosciences*, *35*(8), 1701–1710. https://doi.org/10.1016/j.cageo.2008.06.007

Rice, J. R. (1992). Chapter 20 Fault stress states, pore pressure distributions, and the weakness of the San Andreas fault. In. *International Geophysics*. Elsevier, *51*. https://doi.org/10.1016/S0074-6142(08)62835-1

843 Roland, E., & McGuire, J. J. (2009). Earthquake swarms on transform faults. *Geophysical*
844 *Journal International*, *178*(3), 1677–1690. https://doi.org/10.1111/j.1365-
845 246X.2009.04214.x
846 Ross, Z. E., Kanamori, H., & Hauksson, E. (2017b). Anomalously large complete stress drop
847 during the 2016 Mw5.2 Borrego Springs earthquake inferred by waveform modeling and
848 near-source aftershock deficit. *Geophysical Research Letters*, *44*(12), 5994–6001.
849 https://doi.org/10.1002/2017GL073338
850 Ross, Z. E., Rollins, C., Cochran, E. S., Hauksson, E., Avouac, J. P., & Ben-Zion, Y. (2017a).
851 Aftershocks driven by afterslip and fluid pressure sweeping through a fault-fracture mesh.
852 *Geophysical Research Letters*, *44*(16), 8260–8267. https://doi.org/10.1002/2017GL074634
853 Ross, Z. E., Kanamori, H., Hauksson, E., & Aso, N. (2018). Dissipative intraplate faulting during
854 the 2016 Mw6.2 Tottori, Japan earthquake. *Journal of Geophysical Research: Solid Earth*,
855 *123*(2), 1631–1642. https://doi.org/10.1002/2017JB015077
856 Rossi, G., Zuliani, D., & Fabris, P. (2016). Long-term GNSS measurements from the northern
857 Adria microplate reveal fault-induced fluid mobilization. *Tectonophysics*, *690*, 142–159.
858 https://doi.org/10.1016/j.tecto.2016.04.031
859 Rossi, G., Fabris, P., & Zuliani, D. (2018). Overpressure and Fluid Diffusion Causing Non-
860 hydrological Transient GNSS Displacements. *Pure and Applied Geophysics*, *175*(5), 1869–
861 1888. https://doi.org/10.1007/s00024-017-1712-x
862 Ruhl, C. J., Abercrombie, R. E., Smith, K. D., & Zaliapin, I. (2016). Complex spatiotemporal
863 evolution of the 2008 Mw 4.9 Mogul earthquake swarm (Reno, Nevada): Interplay of fluid
864 and faulting. *Journal of Geophysical Research: Solid Earth*, *121*(11), 8196–8216.

Saiga, A., Matsumoto, S., Uehira, K., Matsushima, T., & Shimizu, H. (2010). Velocity structure in the crust beneath the Kyushu area. *Earth, Planets and Space*, *62*(5), 449–462. https://doi.org/10.5047/eps.2010.02.003

Sato, T., & Hirasawa, T. (1973). Body wave spectra from propagating shear cracks. *Journal of Physics of the Earth*, *21*(4), 415–431. https://doi.org/10.4294/jpe1952.21.415

Scholz, C. H. (1998). Earthquakes and friction laws. *Nature*, *391*(6662), 37–42. https://doi.org/10.1038/34097

Segall, P. (1989). Earthquakes triggered by fluid extraction. *Geology*, *17*(10), 942–946. https://doi.org/10.1130/0091-7613(1989)017<0942:ETBFE>2.3.CO;2

Shapiro, S. A., Huenges, E., & Borm, G. (1997). Estimating the crust permeability from fluid-injection-induced seismic emission at the KTB site. *Geophysical Journal International*, *131*(2), F15–F18. https://doi.org/10.1111/j.1365-246X.1997.tb01215.x

Shelly, D. R., Taira, T., Prejean, S. G., Hill, D. P., & Dreger, D. S. (2015). Fluid-faulting interactions: Fracture-mesh and fault-valve behavior in the February 2014 Mammoth Mountain, California, earthquake swarm. Geophysical Research Letters, 42(14), 5803–5812. https://doi.org/10.1002/2015GL064325

Shelly, D. R., Ellsworth, W. L., & Hill, D. P. (2016). Fluid-faulting evolution in high definition: Connecting fault structure and frequency-magnitude variations during the 2014 Long Valley Caldera, California, earthquake swarm. *Journal of Geophysical Research: Solid Earth*, *121*(3), 1776–1795. https://doi.org/10.1002/2015JB012719

Sibson, R. H. (1992). Implications of fault-valve behaviour for rupture nucleation and recurrence. *Tectonophysics*, *211*(1–4), 283–293. https://doi.org/10.1016/0040-1951(92)90065-E

888 Sibson, R. H. (2020). Preparation zones for large crustal earthquakes consequent on fault-valve
889 action. *Earth, Planets and Space*, *72*(1), 1–20.
890 Talwani, P., & Acree, S. (1985). Pore pressure diffusion and the mechanism of reservoir-induced
891 seismicity. In. *Pure and Applied Geophysics PAGEOPH*. Berlin: Springer, 122(6), (947–
892 965). https://doi.org/10.1007/BF00876395
893 Talwani, P., Chen, L., & Gahalaut, K. (2007). Seismogenic permeability, ks. *Journal of*
894 *Geophysical Research*, *112*(B7), 1–18. https://doi.org/10.1029/2006JB004665
895 Yoshida, K., Saito, T., Emoto, K., Urata, Y., & Sato, D. (2019b). Rupture directivity, stress drop,
896 and hypocenter migration of small- and moderate-sized earthquakes in the Yamagata–
897 Fukushima border swarm triggered by upward pore-pressure migration after the 2011
898 Tohoku-Oki earthquake. *Tectonophysics*, *769*. PubMed: 228184
899 Terakawa, T., Hashimoto, C., & Matsu'ura, M. (2013). Changes in seismic activity following the
900 2011 Tohoku-oki earthquake: Effects of pore fluid pressure. *Earth and Planetary Science*
901 *Letters*, *365*, 17–24. https://doi.org/10.1016/j.epsl.2013.01.017
902 Ueno, H., Hatakeyama, S., Aketagawa, T., Funasaki, J., & Hamada, N. (2002). Improvement of
903 hypocenter determination procedures in the Japan Meteorological Agency. *Quarterly*
904 *Journal of Seismology*, *65*, 123–134.
905 Utsu, T. (1961). A statistical study on the occurrence of aftershocks. *Geophysical Magazine*, *30*,
906 521–605.
907 Utsu, T., Ogata, Y., S, R., & Matsu'ura. (1995). The centenary of the Omori formula for a decay
908 law of aftershock activity. *Journal of Physics of the Earth*, *43*(1), 1–33.
909 https://doi.org/10.4294/jpe1952.43.1

Vidale, J. E., & Shearer, P. M. (2006). A survey of 71 earthquake bursts across southern California: Exploring the role of pore fluid pressure fluctuations and aseismic slip as drivers. *Journal of Geophysical Research: Solid Earth*, *111*(B5), https://doi.org/10.1029/2005JB004034

Waite, G. P., & Smith, R. B. (2002). Seismic evidence for fluid migration accompanying subsidence of the Yellowstone caldera. *Journal of Geophysical Research: Solid Earth*, *107*(B9), ESE 1–ESE 1. https://doi.org/10.1029/2001JB000586

Wada, I., & Behn, M. D. (2015). Focusing of upward fluid migration beneath volcanic arcs: Effect of mineral grain size variation in the mantle wedge. *Geochemistry, Geophysics, Geosystems*, *16*(11), 3905–3923. https://doi.org/10.1002/2015GC005950

Waldhauser, F. (2002). Fault structure and mechanics of the Hayward Fault, California, from double-difference earthquake locations. *Journal of Geophysical Research*, *107*(B3), 2054. https://doi.org/10.1029/2000JB000084

Waldhauser, F., & Ellsworth, W. L. (2000). A double-difference earthquake location algorithm: Method and application to the Northern Hayward fault, California. *Bulletin of the Seismological Society of America*, *90*(6), 1353–1368. https://doi.org/10.1785/0120000006

Wessel, P., & Smith, W. H. F. (1998). New, improved version of generic mapping tools released. *Eos, Transactions American Geophysical Union*, *79*(47), 579–579. https://doi.org/10.1029/98EO00426

Wetzler, N., Lay, T., Brodsky, E. E., & Kanamori, H. (2018). Systematic deficiency of aftershocks in areas of high coseismic slip for large subduction zone earthquakes. *Science Advances*, *4*(2), eaao3225. https://doi.org/10.1126/sciadv.aao3225

932 Woessner, J., Schorlemmer, D., Wiemer, S., & Mai, P. M. (2006). Spatial correlation of
933 aftershock locations and on-fault main shock properties. *Journal of Geophysical Research*,
934 *111*(B8), (B8). https://doi.org/10.1029/2005JB003961
935 Yabe, S., & Ide, S. (2018). Variations in precursory slip behavior resulting from frictional
936 heterogeneity. *Progress in Earth and Planetary Science*, *5*(1), 43.
937 https://doi.org/10.1186/s40645-018-0201-x
938 Yoshida, K., & Hasegawa, A. (2018a). Sendai-Okura earthquake swarm induced by the 2011
939 Tohoku-Oki earthquake in the stress shadow of NE Japan: Detailed fault structure and
940 hypocenter migration. *Tectonophysics*, *733*, 132–147.
941 https://doi.org/10.1016/j.tecto.2017.12.031
942 Yoshida, K., & Hasegawa, A. (2018b). Hypocenter migration and seismicity pattern change in
943 the Yamagata–Fukushima Border, NE Japan, caused by fluid movement and pore pressure
944 variation. *Journal of Geophysical Research: Solid Earth*, *123*(6), 5000–5017.
945 https://doi.org/10.1029/2018JB015468
946 Yoshida, K., Hasegawa, A., & Yoshida, T. (2016a). Temporal variation of frictional strength in
947 an earthquake swarm in NE Japan caused by fluid migration. *Journal of Geophysical*
948 *Research: Solid Earth*, *121*(8), 5953–5965. https://doi.org/10.1002/2016JB013022
949 Yoshida, K., Hasegawa, A., & Okada, T. (2016b). Heterogeneous stress field in the source area
950 of the 2003 M6.4 Northern Miyagi Prefecture, NE Japan, earthquake. *Geophysical Journal*
951 *International*, *206*(1), 408–419. https://doi.org/10.1093/gji/ggw160
952 Yoshida, K., Hasegawa, A., Yoshida, T., & Matsuzawa, T. (2019a). Heterogeneities in stress and
953 strength in tohoku and its relationship with earthquake sequences triggered by the 2011

954 M9 Tohoku-Oki earthquake. *Pure and Applied Geophysics*, *176*(3), 1335–1355.
955 https://doi.org/10.1007/s00024-018-2073-9

956 Yoshida, K., Uchida, N., Hiarahara, S., Nakayama, T., Matsuzawa, T., Okada, T., et al. (2020a).
957 2019 M6. 7 Yamagata-Oki earthquake in the stress shadow of 2011 Tohoku-Oki
958 earthquake: Was it caused by the reduction in fault strength? Tectonophysics, 793,
959 228609.

960 Yoshida, K., Taira, T., Matsumoto, Y., Saito, T., Emoto, K., & Matsuzawa, T. (2020b). Stress
961 release process along an intraplate fault analogous to the plate boundary: A case study of
962 the 2017 M5. 2 Akita-Daisen earthquake, NE Japan. *Journal of Geophysical Research –*
963 *Solid Earth*, e2020JB019527.

964 Yukutake, Y., Ito, H., Honda, R., Harada, M., Tanada, T., & Yoshida, A. (2011). Fluid-induced
965 swarm earthquake sequence revealed by precisely determined hypocenters and focal
966 mechanisms in the 2009 activity at Hakone volcano, Japan. *Journal of Geophysical*
967 *Research*, *116*(B4). https://doi.org/10.1029/2010JB008036

968 Zhao, D., Yanada, T., Hasegawa, A., Umino, N., & Wei, W. (2012). Imaging the subducting slabs
969 and mantle upwelling under the Japan Islands. *Geophysical Journal International*, *190*(2),
970 816–828.

971